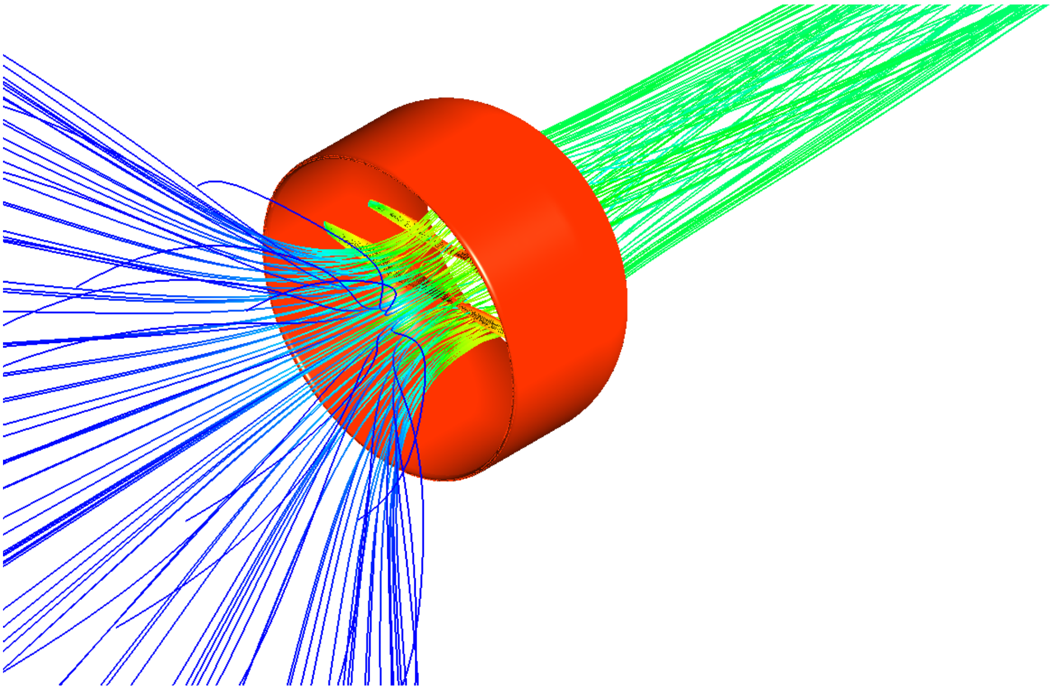

CFD Study on Ducted Rotors for an Urban Air Mobility (UAM) Vehicle

A Performance Validation of Coaxial Rotors for an Urban Air Mobility Vehicle

Master's thesis in Mobility Engineering

Kevin Gnanaraj

Department of Mechanics and Maritime Sciences
CHALMERS UNIVERSITY OF TECHNOLOGY
Gothenburg, Sweden 2024
www.chalmers.se

Master's thesis 2024

CFD Study on Ducted Rotors for an Urban Air Mobility (UAM) Vehicle

A Performance Validation of Coaxial Rotors for an Urban Air Mobility Vehicle

Kevin Gnanaraj

Department of Mechanics and Maritime Sciences
Applied Fluid Dynamics
Chalmers University of Technology
Gothenburg, Sweden 2024

CFD Study on Ducted Rotors for an Urban Air Mobility (UAM) Vehicle
A Performance Validation of Coaxial Rotors for an Urban Air Mobility Vehicle
Kevin Gnanaraj

Supervisor: Patxi Daniel Rodriguez Acero, Department of Mechanics and Maritime Sciences
Examiner: Xin Zhao, Department of Mechanics and Maritime Sciences

Master's Thesis 2024
Department of Mechanics and Maritime Sciences
Applied Fluid Dynamics
Chalmers University of Technology
SE-412 96 Gothenburg
Telephone +46 31 772 1000

Cover: Wind visualization through ducted propellers visualised in CFD-Post, depicting velocity streamlines through the propellers and pressure contours on the surfaces.

Typeset in LaTeX
Printed by Chalmers Reproservice
Gothenburg, Sweden 2024

CFD Study on Ducted Rotors for an Urban Air Mobility (UAM) Vehicle
A Performance Validation of Coaxial Rotors for an Urban Air Mobility Vehicle
Kevin Gnanaraj
Department of Mechanics and Maritime Sciences
Chalmers University of Technology

Abstract

Urban Air Mobility vehicles show promise for use as air ambulances due to the potential to decrease the area footprint of the vehicle, and also facilitates loading from both the side and back of the aircraft, improving vehicle accessibility. Challenges remain in selecting effective propulsion systems for a proposed vehicle to be used in the Västra Götalands region of Sweden, which include the ability of commercial fixed pitch propellers to produce sufficient thrust to ensure safety in case of failure of one of four propulsion units, composed of coaxial rotor pairs in a contra-rotating configuration.

The aerodynamics of propellers is a well studied science, and is relatively simple to predict performance of a propeller given an accurate description of its airfoil geometry from empirical relations. Much research has been done on quantifying the performance of coaxial rotor systems, identifying theoretical empirical limits and advantages of such a configuration, allowing for more limited prediction of performance. Ducted rotors are also well studied in tubomachinery theory, and investigations have been carried out on ducted propellers, but vehicles using coaxial ducted propellers are not as common as unshrouded propellers, and thus this configuration will have to be investigated further to gain an understanding of the factors that affect system performance.

This investigation examines the feasibility of selected propellers to adequately power the proposed vehicle in single, coaxial and ducted configurations through numerical analysis and comparison to experimental data where available, and extending the numerical analysis methodology to untested propulsion configurations.

Results from the investigation revealed that geometrical accuracy of a propeller model is vital to accurately predicting performance of a propeller through numerical analysis, and comparisons to experimental data can help improve the quality of simulated data to extend the analysis to areas where no experimental data is available. This was the case for coaxial simulations, where the results from the single propeller simulation were compared to available experimental data, used to improve the accuracy of the simulation output data, extended to a coaxial configuration, and verified experimentally.

The results also showed that the propellers investigated could meet the thrust requirements for a proposed vehicle under specific conditions in a coaxial configuration, which improved system efficiency over a single propeller, validating the use of numerical simulation of a coaxial propulsion system. The limited duct simulation showed worse performance than a single propeller, but provided a starting point for improved duct design and further numerical analysis.

Keywords: CFD, Coaxial, Commercial, Contra-Rotating, Thrust, shroud, duct, UAM, UAV, Propeller.

Acknowledgements

I would like to thank Patxi Daniel Rogrigeuz Acero, my supervisor, for support with data and providing opportunities to join field-trips that helped develop understanding of aerospace. Xin Zhao, for assistance in setting up simulations on the cluster and other related help. Carlos Xisto, who provided me with a computer that I could use to set up simulations. The good folks at CFD-Online forums who helped me troubleshoot my simulation settings were an immense help.

Kevin Gnanaraj, Gothenburg, August 2024

List of Acronyms

Below is the list of acronyms and initialisms that have been used throughout this thesis listed in alphabetical order:

AMES	Airmobility Emergency System
BEMT	Blade Element Momentum Theory
CAD	Computer Aided Design
CFD	Computational Fluid Dynamics
CW	Clockwise
CCW	Counter-Clockwise
FoM	Figure of Merit
FR	Frozen Rotor
MP	Mixing Planes
MTOW	Maximum Take-Off Weight
RPM	Rotations Per Minute
SST	Shear Stress Transport
UAM	Urban Air Mobility
UAV	Unmanned Aerial Vehicle

Nomenclature

Below is the nomenclature of indices, parameters, and variables that have been used throughout this thesis.

Indices

j	Indices for axis direction in tensor notation

Parameters

α, β, β^*	Closure coefficients
D	Propeller diameter
ζ	Bulk viscosity of fluid
k	Thermal conductivity of fluid
μ	Fluid dynamic viscosity
ν	Fluid kinematic viscosity
ν_T	Fluid kinematic turbulent viscosity
∇	Divergence operator to decompose vector variable to scalar variables
R	Fluid gas constant
ρ	Fluid density
σ_k, σ_ω, $\sigma_{\omega 2}$	Closure coefficients
Φ	Viscous dissipation
$\square^T$	Matrix transpose operation

CFD Variables

$\boldsymbol{f}$	Body forces acting on fluid

F_1	Blending function for wall distance
p	Pressure
P_k	Production term for turbulent kinetic energy
P_ω	Production term for dissipation of kinetic energy
t	Time
T	Fluid temperature
$\boldsymbol{u}$	Fluid velocity vector
U_j	Velocity of fluid, tensor notation
$\boldsymbol{\Omega}$	Angular velocity vector

Propeller Performance Variables

c_P	Coefficient of power
c_Q	Coefficient of torque
c_T	Coefficient of thrust
FoM	Figure of Merit
κ_{int}	Rotor interference factor
n	Rotational speed, rotations per second
P_{in}	Power input, measured at shaft
Q	Torque
T	Thrust
T_u	Thrust, upper rotor
T_l	Thrust, lower rotor

Contents

List of Figures

List of Tables

1

Introduction

The rapid development of miniaturised electronics along with reduced costs has enabled the spread of unmanned aerial vehicles (UAVs) to the general public, where it was limited to people with interest in learning the flight mechanics required to fly such vehicles. Now, due to the control simplifications enabled using microprocessors, UAVs, also known as drones, are easily operable by laypersons to flight control, as this has been abstracted away by manufacturers of drones.

This allows for a range of use cases, such as improved emergency medical response, investigated in this report. Most drones, however, are small scale [1], and are typically not intended to be used to carry people as payloads, though this is an active area of development worldwide. Medical airlift is generally carried out using helicopters, which are rated for conveyance of people, and have been doing so for many years.

One identifiable safety reason for this is that helicopters can auto-rotate their propellers in the event of a power failure, a technique unavailable to drones due to the fixed-pitch (fixed angle of attack) propellers typically used in their construction. Helicopters work by adjusting propeller angle of attack for flight control, while drones generally rely on adjustments in propulsive output for flight control.

An example of a helicopter used as an air ambulance can be seen in figure 1.1.

Figure 1.1: Helicopter used by Svensk Luftambulans as air ambulance. By Klas Sjöberg [2]

The challenges behind the propulsion design using coaxial contra-rotating rotors for such a vehicle are investigated in this report.

1.1 Project Background

The Airmobility Emergency System (AMES) Project is an initiative to develop an air ambulance for Västra Götalands Regionen, Sweden in partnership with multiple organisations in the region representing different interests. AMES aims to develop a Urban Air Mobility (UAM) vehicle using UAV technology, with the goal of reducing emergency response times and increasing accessibility by reducing the physical footprint of the system.

The proposed vehicle has the following target specifications:

- 800 kg Maximum Take-Off Weight (MTOW)
- 250 kg Payload
- 15-20 minute hovering time
- 2.5 m tall, 6 m long, 2.3 m wide (without rotors)

In pursuit of the project's goals, a UAV has been designed with 4 coaxial contra-rotating pairs, seen in fig 1.2.

Figure 1.2: Concept image of UAM vehicle for AMES

This configuration has its advantages and challenges, which are discussed here.

1.1.1 Advantages

There are three main advantages to the design of the vehicle that give it certain advantages over a helicopter air ambulance, all related to the use of multiple rotors, as shown in the concept in figure 1.2.

- The use of multiple rotors can reduce the overall area footprint of the vehicle through the use of smaller rotors that can generate the same thrust that a single, much larger helicopter rotor would require.
- The use of multiple rotors, especially when used in even numbers, removes the need for the tail rotor typically found on helicopters, which is used to counteract the rotation induced by the torque required by the main rotor, which further reduces the area footprint.
- Along with the shrouded blades, which can improve efficiency, the removal of the tail rotor can allow loading from the rear, which is usually not possible with medical helicopters, with notable exceptions of military helicopters such as the CH-47 Chinook [3], with tandem rotors. This can improve accessibility in spaces where loading from the side may not be possible, or could be slower than rear loading.

1.1.2 Challenges

While there some advantages, as noted, the design of a fixed pitch propeller vehicle for human transport, especially medical airlift, brings challenges. Safety is the most important factor in this aircraft design, as an unsafe ambulance can cause additional harm. The following points are major areas of challenge.

- The loss of the ability to auto-rotate in the event of a power failure is a major concern. The vehicle should have some way to ensure that the occupants can exit safely in this case.
- The high speed propeller blades. In order to generate the same thrust as a much larger helicopter blade, the propellers will spin at higher rotational speeds than a helicopter rotor, about 5-10 times faster, and thus more sensitive to imbalances. Any imbalances that cause the blades to spin erratically can cause them to break and fly out due to centripetal forces. This can occur from defective rotor blade manufacture, or foreign object damage. Combined with the fact that there will be 8 sets of blades, there is more potential for catastrophic failure.
- This danger from failing blades can in part be mitigated by a shroud, but a stronger shroud will likely incur weight penalties that must be accounted for in some way, and negate the thrust generation advantages that could be gained from using the shroud.

1.2 Purpose of investigation

The purpose of this investigation is to validate that a coaxial configuration using selected commercially available propeller models will be able to generate the thrust required to lift the MTOW of the proof-of-concept prototypes for the air ambulance, at a small scale with a MTOW of 25 kg, and a full scale prototype with a MTOW of 800 kg, using numerical simulation.

The results of the investigation will be verified experimentally at the small scale, and used to assist in selection of appropriate propeller models for the full scale prototype.

To address a key safety concern, the design of the vehicle has been adapted so that 3 of the 4 rotor pairs will bear the designed maximum total weight of 800 kg, in the case that one set of rotors ceases to function. This is to account for the fact that auto-rotation is not possible, so a degree of redundancy has to be built in for safety reasons.

To understand whether the coaxial system is capable of producing the required thrust, an understanding of the theory behind thrust generation is required. A literature survey follows, and the next chapter goes into more detail of the theory behind the present propeller analysis.

1.3 Literature Review

Coaxial propellers are not a novel technology, as they can be found on many types of vehicles, from large planes like the Tupolev Tu-116 and helicopters such as the Kamov Ka-52, seen in figure 1.3, to contemporary drones such as the T-Drone MX680 [4]

(a) Tu-116. By Andrey Mossejev [5]   **(b)** Ka-50. By VlSergey [6]

Figure 1.3: Examples of aircraft employing coaxial rotors for propulsion

There have been multiple studies on the aerodynamic characteristics of propeller performance, similar to what is being investigated here. A starting point to look at would be Patrao's doctoral thesis on boxprop design [7], which outlines methodology that can be used to set up the Computational Fluid Dynamics (CFD) model for propellers, and the reasoning behind it. The CFD model employed here is the k-ω Shear Stress Transport (SST) turbulence model, which adjusts the turbulence model based on wall distance using a blending function, to improve accuracy of turbulence modelling by employing the more appropriate model.

Stajuda et al. [8] study the importance of using appropriate domain sizes to ensure that flow features are not lost in transition between the rotating and stationary domains. The study found that thicker disks for the rotating domain captured the results of the flow more accurately at higher rotational speeds.

Loureiro et al. carried out a study [9] on simulations of small propellers to evaluate their performance. This paper suggests dimensions for the computational domain parameterised by the propeller diameter, while comparing two different simulation methods (Blade Element Momentum Theory (BEMT) (implemented in QProp and JBLADE) and CFD (implemented in ANSYS CFX and OpenFOAM)), two different turbulence models (k-ω SST and SST $\gamma - \theta$), using their respective mesh interfaces (Frozen Rotor (FR) in CFX and Arbitrary Mesh Interface in OpenFOAM). However, the inlet conditions are for a propeller in motion through air, rather than a static thrust evaluation, as are of interest. The propeller geometry investigated was an APC 14x7e propeller, and the geometry obtained using 3D scanning and CAD modelling. The results showed that the FR simulations overpredict thrust at lower advance ratio values compared to the experimental data, but converging with other methods at higher advance ratios. The different BEMT methods diverge at higher values of advance ratio.

Another study by Kutty and Rajendran [10] carries out an investigation using the APC 10x7 propeller as the geometry. Simulations of single propeller showed good agreement with experimental data, with accuracy of simulations increasing with RPM. The domain dimensions were similar to Loureiro et al.'s study, but the outer stationary domain used a cuboid instead of a cylinder. The simulation was conducted using ANSYS Fluent. This study also used boundary conditions for a propeller moving in air.

Panjwani et al. have carried out a study [11] that carries out a very similar investigation that is intended to be used for reducing the need for static thrust experiments through validation of thrust simulation models. Using 5 different propellers (APC 10 x 7, APC 11 x 7, and three undiclosed models), they carried out numerical analysis using scanned propeller geometry. The airfoils and their lift and drag coefficients were predicted using QBlade, which was then used to generate a CFD-BEMT model for simulation of performance, which was then compared to experimental data. Their results highlight the need for accurate blade geometry in numerical simulation, since pure CFD simulations underpredicted performance. The factor of underperformance was consistent enough that a multiplication factor could be applied to the simulated thrust to approximately match the experimental data for each propeller. However, this approach still underpredicted the thrust at higher rotational speeds.

From the work done in these papers collected, an idea of the theory, discussed in the next chapter, and the methodology in the following chapter, can be formed to carry out the investigation of thrust of a coaxial propeller system using numerical analysis. The assumptions used to justify the theory and methodology used are outlined before moving on to them.

1.4 Assumptions

Many different propellers exist for a range of different flight missions. Even within a given flight profile, the requirements on the propulsion can change. However, there will be mission critical scenarios where the propulsion system must perform its duty, otherwise the whole system will not be viable. This scenario determines the viability of the propulsion system investigated for the air ambulance, and its scope and constraints.

The AMES design has set this point as hovering flight at 60% of any limitations such as propulsion system power delivery capability, tip Mach number etc., (assuming only 3 propeller pairs are functional) outside of the ground-effect region, so that there will be enough excess power to translate the aircraft horizontally in any direction by shifting power to different propeller sets, as well as moving to higher altitudes. This translates to the following assumptions for the investigation that simplify simulation conditions:

- Steady state, since sustained thrust is the most important value under investigation
- Compressible flow, as tip mach numbers of the propellers are expected to exceed 0.3
- Constant angle of attack, because the propulsion is being evaluated for hover performance
- Fixed geometry, the propellers cannot move their position independently of the vehicle

2

Theory

The principles of propeller performance can be defined using BEMT, which can also be used in conjunction with known properties of given airfoils to predict real performance. While these equations are defined in two dimensions, along the radius of the propeller they can be combined to predict 3D performance. This may be used by manufacturers of propellers to provide performance estimates of their products, such as the propellers investigated in the present report.

The performance of a given propeller geometry can be investigated using CFD, which solves the fluid flow equations around a propeller blade, and from these solutions, can be used to simulate the performance of the propeller under strictly controlled conditions, based on boundary conditions used. This is the method employed in this report, and the theory behind the CFD used in the simulations is discussed here.

2.1 Equations of Fluid Flow in CFD

The characteristics of a given fluid flow can be defined by a series of conservation equations for mass, momentum and energy, as well as the equation of state and they are written as follows in the general form, for a compressible flow [12].

2.1.1 Continuity equation (mass conservation)

$$\frac{\partial \rho}{\partial t} + \nabla \cdot (\rho \mathbf{u}) = 0 \tag{2.1}$$

The continuity equation represents the mass flow in and out of the system, with conservation enforcing that flow into a domain must equal the flow out of it. It consists of the following quantities:

- ρ - density
- t - time
- $\boldsymbol{u}$ - velocity vector of fluid
- ∇ - divergence operator, decompose vector into scalar components

2.1.2 Navier-Stokes equation (momentum conservation)

$$\rho\left(\frac{\partial \boldsymbol{u}}{\partial t}+(\boldsymbol{u}\cdot\nabla)\boldsymbol{u}\right)= -\nabla p+\nabla\cdot\left\{\mu\left[\nabla\boldsymbol{u}+(\nabla\boldsymbol{u})^T-\frac{2}{3}(\nabla\cdot\boldsymbol{u})\right]\right\}+\nabla\left[\zeta\left(\nabla\cdot\boldsymbol{u}\right)\right]+\rho\boldsymbol{f} \quad (2.2)$$

The Navier-Stokes equations represent the change of momentum within the system, and like the continuity equation, ensures conservation of momentum in the domain, that is, the total sum of momentum in the domain studied must equal zero. The equation introduces a few additional variables over the continuity equation:

- p - pressure
- μ - dynamic viscosity of the fluid
- T - transpose operation of matrix
- ζ - bulk viscosity of fluid, representing resistance to volume change of the fluid
- $\boldsymbol{f}$ - body forces acting on the fluid, such as gravity

2.1.3 Conservation of energy

$$\rho\left(\frac{\partial}{\partial t}+(\boldsymbol{u}\cdot\nabla)\right)h = \left(\frac{\partial}{\partial t}+(\boldsymbol{u}\cdot\nabla)\right)p + \nabla\cdot(k\nabla T) + \Phi \quad (2.3)$$

Likewise, the conservation of energy tracks the total energy contained in the system, and in a closed system, it should sum to zero. In the conservation of energy equation,

- k - thermal conductivity of fluid
- T - temperature of fluid
- Φ - viscous dissipation, the rate of conversion of energy to heat

Because the flow investigated is compressible, the state equation to track the change of density of the fluid must also be included in calculations [12]. The equation of state is given by:

$$p=\rho RT \quad (2.4)$$

where R is the gas constant of the fluid, which in our case is air.

2.1.4 Equation reduction

Since the value of highest interest is the sustained thrust, or force, of the propellers, the problem is assumed steady-state, and thus equations 2.1, 2.2, and 2.3 reduce to the following forms from the removal of time-related change terms:

- Continuity equation (mass conservation)

$$\nabla\cdot(\rho\mathbf{v})=0 \quad (2.5)$$

- Navier-Stokes equation (momentum conservation)

$$\rho\left((\boldsymbol{u}\cdot\nabla)\boldsymbol{u}\right)= -\nabla p+\nabla\cdot\left\{\mu\left[\nabla\boldsymbol{u}+(\nabla\boldsymbol{u})^T-\frac{2}{3}(\nabla\cdot\boldsymbol{u})\right]\right\}+\nabla\left[\zeta\left(\nabla\cdot\boldsymbol{u}\right)\right]+\rho\boldsymbol{f} \quad (2.6)$$

- Conservation of energy

$$\rho(\boldsymbol{u} \cdot \nabla)h = (\boldsymbol{u} \cdot \nabla)p + \nabla \cdot (k\nabla T) + \Phi \tag{2.7}$$

These equations are used to calculate the fluid flow properties in a domain of interest, which, in this case, is a rotating propeller surrounded by a fixed volume of still air. The domain is divided into elements of varying shapes and sizes to capture the local flow properties and the equations are applied to each element. As the number of elements can become very large, the computational requirements become very high, and thus simplifications to the domain are applied to reduce computational complexity, reducing the time required to get results, which will sacrifice accuracy by a certain amount.

2.1.5 Frames of reference

The momentum equation 2.6 assumes a stationary frame of reference. However, since propellers rotate, they experience pseudo-forces resulting from the angular velocity, giving it the form:

$$\begin{aligned}\rho\left((\boldsymbol{u} \cdot \nabla)\boldsymbol{u}\right) = -\nabla p + \nabla \cdot \left\{\mu\left[\nabla \boldsymbol{u} + (\nabla \boldsymbol{u})^T - \frac{2}{3}(\nabla \cdot \boldsymbol{u})\boldsymbol{I}\right]\right\} \\ + \nabla\left[\zeta\left(\nabla \cdot \boldsymbol{u}\right)\right] + \rho \boldsymbol{f} - \rho\left[2\boldsymbol{\Omega} \times \boldsymbol{u} + \boldsymbol{\Omega} \times (\boldsymbol{\Omega} \times \boldsymbol{x})\right]\end{aligned} \tag{2.8}$$

where $\boldsymbol{\Omega}$ is the angular velocity of the rotating frame, and $\boldsymbol{x}$ is the position of a fluid element [13].

Domain motion must be accounted for, as the fluids in motion will have have a difference reference frame than those in a stationary domain. Equation 2.8 is used in a rotating frame of reference, and is the momentum seen by the fluid within the rotating frame. There are multiple methods used to interface rotating domains with stationary domains and other rotating domains. The type of frame change used can affect the results by the transition of the flow between the domains.

2.1.5.1 Frozen Rotor

The frozen rotor (FR) domain interface implements a fixed relative position of the rotating frame to the stationary frame of reference, and a frame transformation, much like that seen in equation 2.8 is applied to simulate motion. However, due to the fixed relative positive, transient effects are lost, and any transient flow properties resulting from relative positions (such as rotor-stator interactions in a jet engine) remain static.

2.1.5.2 Mixing Planes (Stage)

Another method is the mixing planes interface, also known as stage, where flow properties are averaged circumferentially for a given radius between frames of reference. This can reduce computation costs significantly, as only a single blade row needs to be simulated, but at the loss of transient flow interactions such as rotor-stator interactions. [14]

Another aspect that is not captured easily is turbulence in flow, which is computationally expensive, and is thus modelled. One such model is the $k-\omega$ SST model, which is a well-known turbulence model used to capture the transport of energy in turbulent parts of the flow.

2.1.6 $k-\omega$ SST model

The $k-\omega$ SST model uses a two equation model to capture the effects of turbulence through two transport variable, k, which is turbulent kinetic energy, and ω, which is turbulence dissipation rate. The Shear Stress Transport (SST) portion of the model uses a blending function to switch between the $k-\varepsilon$ turbulence model away from wall regions, in free stream conditions, where it performs better than the $k-\omega$ turbulence model. Near wall regions, due to its ability to handle adverse pressure gradients well, the $k-\omega$ is used. [15]
The two equations are of the form [16] seen in equations 2.9 and 2.10.

2.1.6.1 k equation

$$\frac{\partial k}{\partial t} + U_j \frac{\partial k}{\partial x_j} = P_k - \beta^* k\omega + \frac{\partial}{\partial x_j}\left[(\nu + \sigma_k \nu_T)\frac{\partial k}{\partial x_j}\right] \tag{2.9}$$

where P_k is the production term for turbulent kinetic energy, β^*, σ_k are coefficients of closure, defined by Menter [15], ν and ν_T are kinematic viscosity and kinematic turbulent viscosity respectively. The x_j term represents positions of fluid elements in the domain using tensor index notation, where j can represent one of the coordinate axes during computation.

2.1.6.2 ω equation

$$\frac{\partial \omega}{\partial t} + U_j \frac{\partial \omega}{\partial x_j} = \alpha \frac{P_\omega}{\nu_T} - \beta \omega^2 + \frac{\partial}{\partial x_j}\left[(\nu + \sigma_\omega \nu_T)\frac{\partial \omega}{\partial x_j}\right] + 2(1 - F_1)\sigma_{\omega 2}\frac{1}{\omega}\frac{\partial k}{\partial x_i}\frac{\partial \omega}{\partial x_i} \tag{2.10}$$

where P_ω is the dissipation production term, U_j is the instantaneous velocity in the x_j direction, α, β, σ_ω and $\sigma_{\omega 2}$ are again coefficients of closure as defined by Menter [15], and F_1 is the blending function that computes wall distance to determine which turbulence model to apply.

2.2 Propeller Performance Evaluation

The performance of the propellers evaluated in CFD can be evaluated, as previously mentioned, by Blade Element Momentum Theory (BEMT) [17]. While BEMT can be used to predict and evaluate the specific performance along a blade's radius, the performance of interest in this investigation is the overall performance of the propeller, specifically thrust. Thus the equations related to overall performance derived from BEMT are discussed here.

To compare propellers of varying geometry from different manufacturers, dimensionless variables are essential, in order to normalise the variables and investigate those of highest interest methodically.

2.2.1 Thrust

Since thrust is the performance variable of most interest in this investigation, a dimensionless value of thrust, called the coefficient of thrust, denoted by c_T is used. It is given with the formula:

$$c_T = \frac{T}{\rho n^2 D^4} \tag{2.11}$$

where T is the thrust generated by the propeller, ρ is the ambient air density, n is the rotation speed in revolutions per second, and D is the propeller diameter. c_T can be used to compare the performance across propellers while normalising propeller diameter and rotational speed.

While thrust is the most important performance parameter here, the torque required to drive the propeller is an important consideration, because it will determine the motor that will drive the propeller to the required rotational speed to produce the thrust required. This can be compared using another dimensionless variable.

2.2.2 Torque

The coefficient of torque, c_Q is given by the equation

$$c_Q = \frac{Q}{\rho n^2 D^5} \tag{2.12}$$

Where Q is torque. This can be used to compared the torque required to produce a given thrust while controlling for diameter and rotational speed, and can be an indirect measure of efficiency.

2.2.3 Power

Another indirect measure of efficiency is power input (P_{in}), measured at the shaft, as a function of the torque ($P_{in} = 2\pi n Q$). It is non-dimensionalised as c_P and can be calculated using the following formulae.

$$c_P = 2\pi c_Q \tag{2.13a}$$

$$c_P = \frac{P_{in}}{\rho n^3 D^5} \tag{2.13b}$$

These variables measure the power input directly, and can be used to estimate the input requirements for the propeller to produce a given thrust. To measure the efficiency, a ratio of input power to output thrust is required.

2.2.4 Hover Efficiency

Using BEMT to calculate propeller efficiency for hover conditions is not directly possible, since it involves the use of a dimensionless variable J, known as the advance ratio, which assumes forward flight velocity, which in the present case is zero. Another variable, the Figure of Merit (FoM) is used, and it has been defined for rotors in hover conditions [18] [19]. It can be defined by either the torque or power coefficients.

$$FoM = \frac{c_T^{3/2}}{\sqrt{2}c_Q} \tag{2.14a}$$

$$FoM = \frac{c_T^{3/2}}{\sqrt{2}c_P} \tag{2.14b}$$

The equations 2.14 can be used to evaluate the FoM for either single or coaxial rotor configurations, with the coaxial power as the simple sum of both the rotors' power inputs.

Leishman [20][21] argues that this definition violates the blade loading assumption implicit in the definition that the rotors take all of the disk loading of the system, which is not true for coaxial systems, and proposes a new formulation that attempts to address this. This formulation found in his paper [21] and book [20] will not be used in this report for simplicity, and because it requires the knowledge of airfoil characteristics which are not given for the propellers investigated.

2.2.5 Coaxial performance

Ideally, adding a second rotor co-axially would double the performance of a propulsion system. But this is not the case due to airflow patterns and the interference with the second rotor. This interference can be quantified and used to gain a measure of the performance when rotors are used co-axially, using an interference factor κ_{int}, defined by Leishman [20]. It is given by the formula:

$$\kappa_{int} = 2\sqrt{2}\left(\frac{T_u}{T_l}\right)^{3/2}\left(1 + \frac{T_u}{T_l}\right)^{-3/2} \tag{2.15}$$

where T_u is the thrust generated by the upper rotor and T_l is the thrust generated by the lower rotor. For a coaxial rotor pair operating at the same torque, κ_{int} is expected to have a value of 1.281 [20]. This is the expected operating condition for the prototype in hover.

Using the theory defined in this chapter, the methodology used to collect the data to validate the performance using CFD, and to experimentally test the propellers is explained in the next chapter.

3

Methods

As stated in the introduction, two propeller models were tested in CFD, a smaller propeller model for the systems test prototype, and a proposed propeller model for the full-scale prototype to validate their performance and verify that they will provide the required thrust for the stated condition of 60% of limiting factors. The two propellers used were the T-motor NS 22x6.6 [22], which is a 22 inch diameter propeller with a pitch of 6.6 inches (i.e. 6.6 inches is moved along rotation axis for every full revolution) intended for use with the systems test prototype, and a Mejzlik Propellers Propeller 60x21 2B MC [23], with a diameter of 60 inches and a pitch of 21 inches, intended for use with the full-scale air ambulance prototype.

Numerical simulations for both propellers were carried out and compared to experimental data in a single rotor configuration, and compared with performance data, obtained from the manufacturer and independent sources where available. In the case of the NS 22x6.6, experimental data was available from Tyto Robotics' online database [24] for performance, but it must be noted that this data is unverified and does not contain error margins. Additionally, for the Mejzlik propeller, the manufacturer provided data is extrapolated after 1600 RPM. The data from manufacturers can be found in the appendices of this report. Manufacturer data for the T-Motor propeller is obtained at 9 °C, which will affect air density which in turn affects propeller performance.

To validate the performance of the propellers, a model was setup to compare simulated data to experimental data for a single propeller. This is to ensure that the simulation is accurate and can predict the performance of the propeller in a coaxial configuration.

Since coaxial data is not expected to be available, the simulation results for the small T-motor propeller were compared to in-house experimental tests with the actual propeller. No experimental data is known to be available at the time of writing for the Mejzlik propeller in a coaxial configuration.

The particular propeller testing and simulation methodology is discussed now.

3.1 Numerical Simulation

To simulate the thrust on the propeller system, ANSYS CFX was used. It was chosen because similarities of the problem to turbomachinery, that CFX is commonly used for, are present in the problem. These include multiple rotating domains, and though taken out of the scope of this present investigation, the shroud enclosing the rotors. Full 3D simulations were carried out, without the use of symmetries, due to difficulties in the setup of rotational symmetry.

3.1.1 CFD Setup

3.1.1.1 Domain setup

In order to simulate the expected test conditions as closely as possible, the stationary simulation domain was set to have openings for inlets and outlets, with a reference pressure of 0 atm, and a reference temperature of 25 °C. Within the domain, the temperature was also set to be 25 °C, but the pressure was set to 1 atm. Total energy was turned on, to capture compressibility effects, since the propeller tips were expected to be moving faster than Mach 0.3 at the highest rotational speed. It should be noted that this may not capture transonic losses that are expected at speeds higher than Mach 0.8 due to compressibility effects [25], which are expected at the tip for the larger propeller model.

The sizes of the rotating domains were based on similar propeller studies seen in the literature review [9][10], with the stationary domain being a cuboid with sides of 8 propeller diameters (8D) on all sides for the single propeller simulations, and an addition of assumed motor size (M_z) to define spacing for the coaxial rotor simulations (8D + M_z). The rotating domains for the propellers were set to be at the geometric centre of the stationary domain,

The rotating domain size was also selected based on the studies in the literature review, modelled as cylinders with a diameter of 1.1D for the Mejzlik propeller and 1.2D for the T-motor propeller (the discrepancy was discovered late after all simulations were done), and a length of 0.4D for the single rotor, while the coaxial rotor had a length of 0.4D + M_z, while keeping the same diameter. A cylinder was cut out of the domains to represent the motor for the coaxial simulations, and set as a no-slip, smooth wall. The propeller blades were also setup in the domain similarly, as a smooth no-slip wall. A quick test using the Mejzlik propeller at 3000 RPM revealed that the difference in thrust when using a rotating domain size of 1.2D compared to 1.1D is only 0.01%, and 0.1% when comparing torque between the two domain sizes.

M_z for the T-Motor propeller was assumed to be 0.140 m and 0.300 m for the Mejzlik propeller, based on the approximate size of the coaxial motor housing measured on site for the T-Motor propeller.

Due to time limitations, a very limited simulation of a shrouded coaxial propeller test of the Mejzlik propeller was carried out, yielding a single data point. As much geometry from the coaxial setup was used as possible, with the total length of the propeller domains remaining at 0.4D + M_z, and the shroud starting at a diameter of 1.1D and a thickness of 0.01 m. The exit was set to have an area of 0.9D to act as a converging duct. An elliptical lip protrusion with a length of 0.02 m was created for the intake.

The rotating domains were set to have a frozen rotor interface with the stationary domain, and a mixing plane interface with each other. As explained in the theory, this means that the stationary domain sees the rotors in a fixed relative position, and using the equations in 2.8 within the propeller domains, motion is simulated. Between the rotating domains, the relative blade motion is simulated using a mixing

plane interface, but flow details such as tip vortices will be lost due to the averaging of the flow properties.
Representative 2D and 3D diagrams (not to scale) can be seen of the simulation domains following.

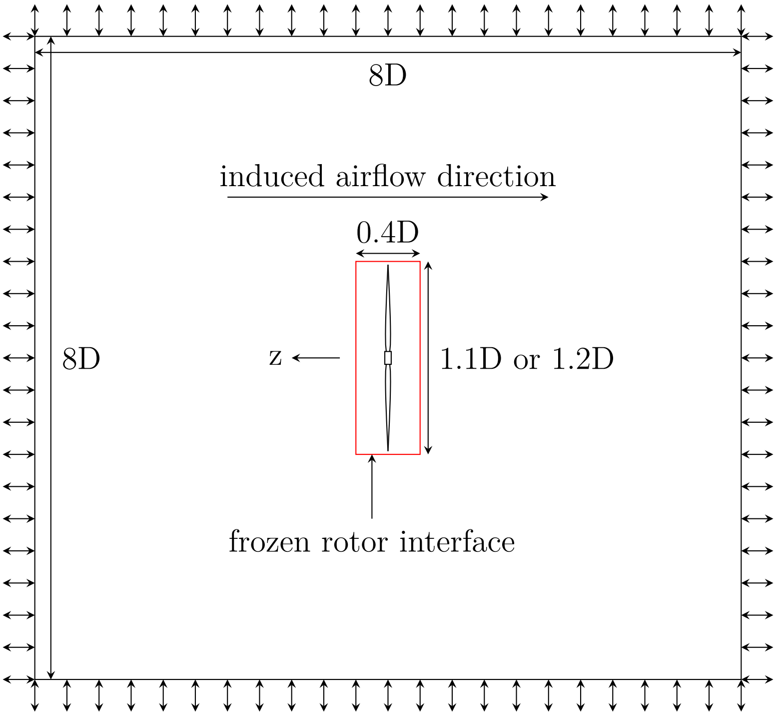

Figure 3.1: Single propeller CFD setup representation, 2D representation

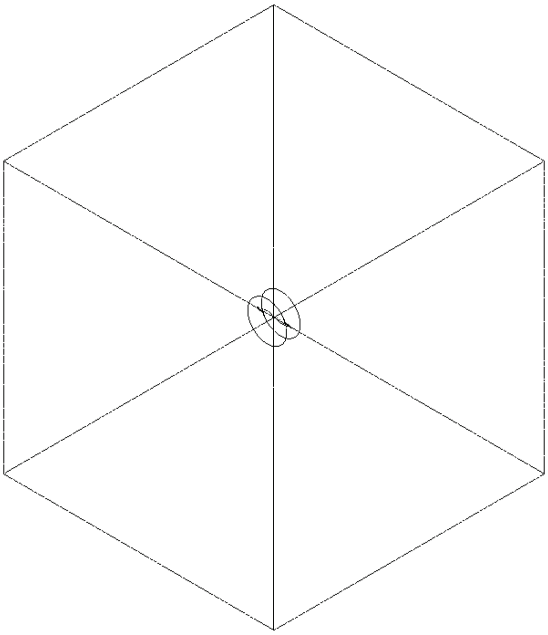

Figure 3.2: 3D CFD domain of single propeller

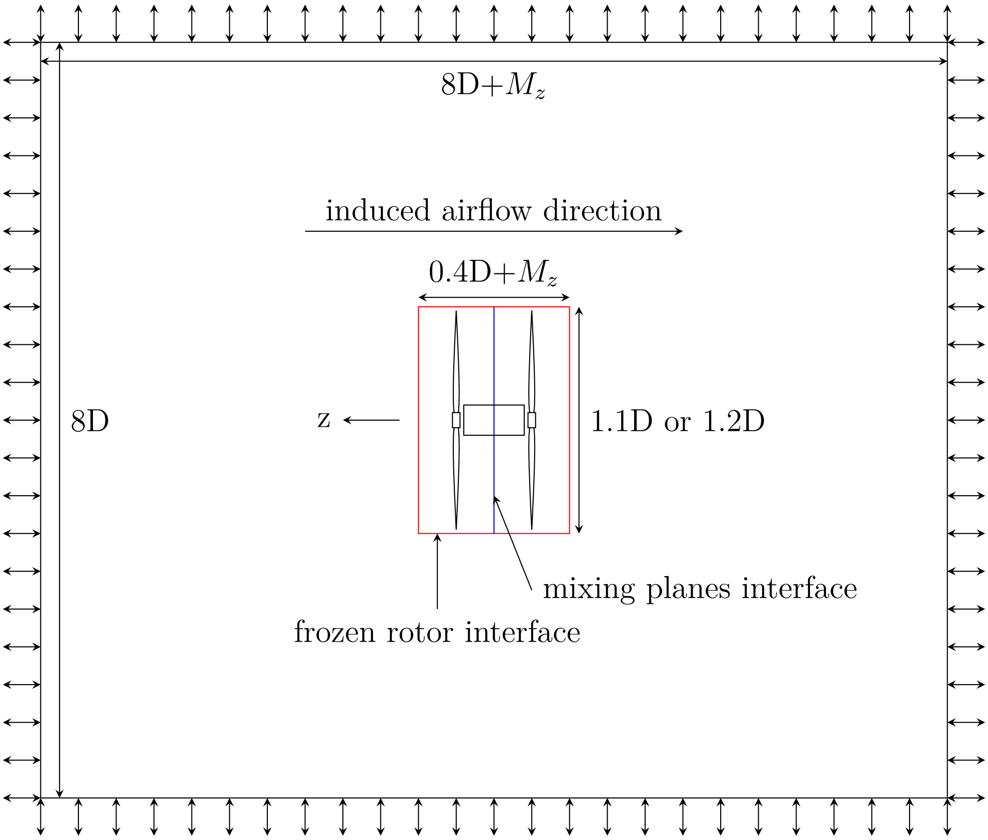

Figure 3.3: Coaxial configuration CFD setup, 2D representation

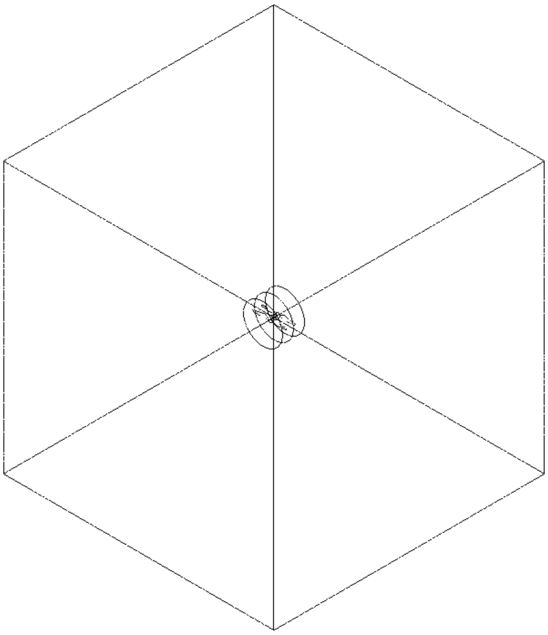

Figure 3.4: 3D CFD domain of coaxial propellers

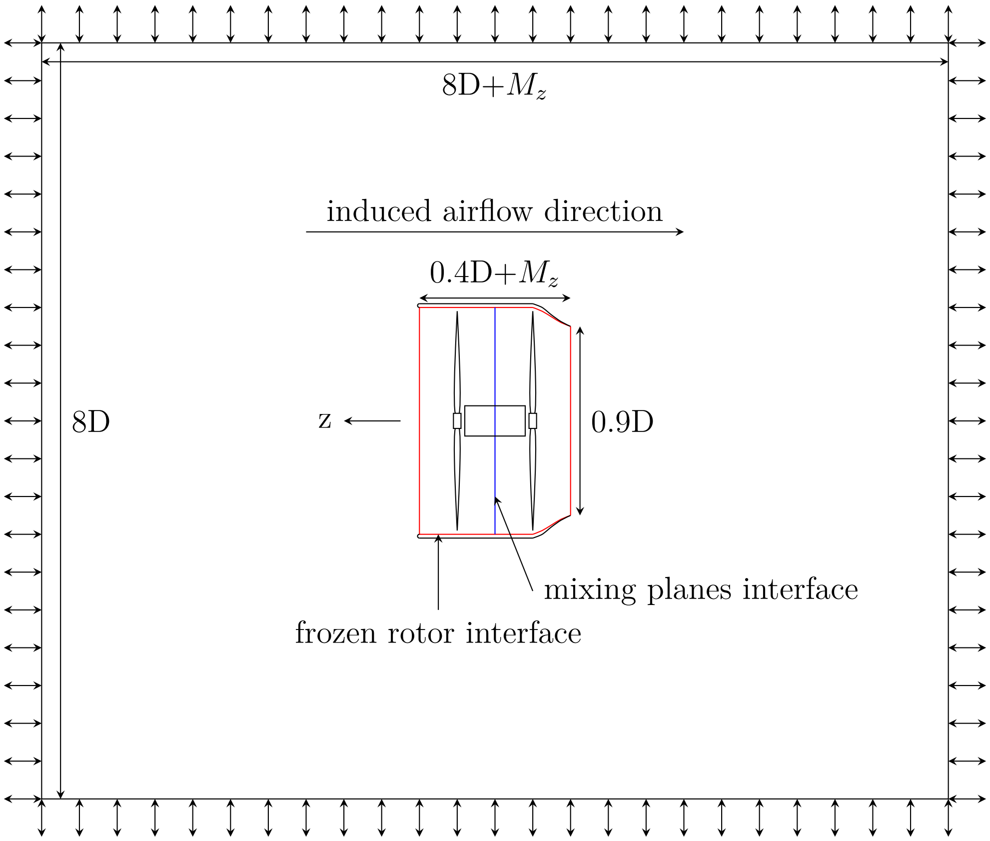

Figure 3.5: Coaxial configuration with shroud CFD setup, 2D representation

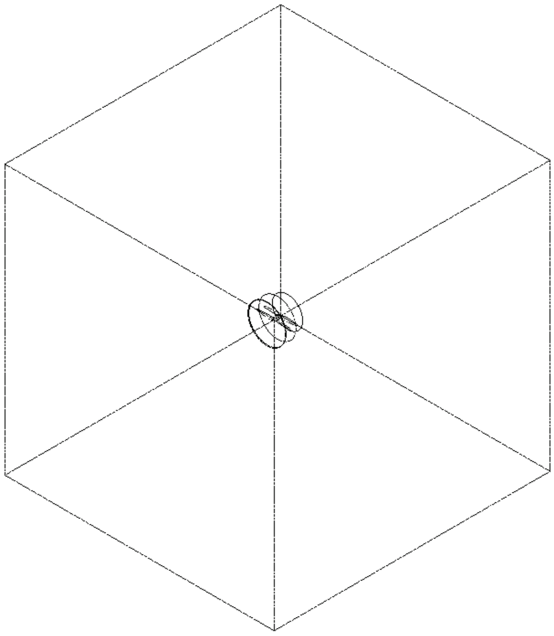

Figure 3.6: 3D CFD domain of shrouded coaxial propellers

3.1.1.2 Mesh generation

A mesh that captures an acceptable level of accuracy while still allowing resolution of the flow equations within a reasonable time requires a grid independence study, to ensure that the results are independent of the mesh itself. To begin with, all the default mesh settings in ANSYS' mesh software were used for all domains. Structured meshes with cubic elements were generated at the start, in order to reduce element count, however the meshes failed to generate after 2 refinement steps, so unstructured meshes were used from that case. The refinement was carried out by approximately halving the base element length and targeting an increase of 5-8 times the previous element count, until the change in target output value (thrust coefficient in this case) between mesh refinements stops increasing.

The grid study was carried out using a single propeller configuration of the T-motor NS 22x6.6 propeller. The refinement was first done on the stationary domain, and then using the most acceptable mesh, the rotating domain domain was refined until the results were suitably independent from the mesh. In order to capture the boundary layer effects on the blade, inflation with 10 layers, and a smaller cell size (approximately half the domain base size, but tuned to keep the overall domain domain cell count in the target range) at the surface of the rotor blades. Tip refinement was attempted to capture compressibility effects due to high Mach numbers, but mesh generation failed, so that level of detail was abandoned to save time.

The refinement was based on the difference from the independent experimental data of the simulation data of the thrust. The selected mesh was based on the smallest change in thrust differences between mesh refinement steps.

The RPM used for the grid study was the highest used for the experimental data available - 4471.

Using the results from the grid study, a similar mesh size was used for the larger Mejzlik propeller, with settings to target a similar element count.

Table 3.1: Test matrix for grid independence study

Mesh	Elements		
	Domain	Propeller	
default	4513	1500579	
coarse	24108	1500579	
fine	186057	1500579	
finer	1458852	1500579	
very fine	8955797	1500579	
superfine	57064915	1500579	
improved	8955797	1864793	
fine	8955797	12042299	
fine	8955797	12042299	High turbulence outlet
very fine	8955797	62479005	

3.1.1.3 Thrust validation test matrix

The simulation input test variables were the RPM values, since that would be the variable that best determines the level of performance that could be expected from the propellers, and also defines the limitations of the propulsion system. The test matrix for the propellers was based on independent experimental data [24] for the small T-motor model, and from manufacturer provided data for the Mejzlik model. These datasets were compared with the simulation results to determine the level of accuracy of the simulation, and to evaluate the expected performance of the propellers. The exact RPM values simulated can be seen in Table 3.2. The values highlighted in orange were only simulated and had no experimental data available. The values extracted from the simulation were total force on planes placed on the exits of the propeller domains and the torque on each rotor. From these two values, and the input RPM, all other performance values indicated in section 2.2 were calculated, as well as the tip Mach number, as it is a constraining factor. In addition, pressure and velocity contour plots, as well as velocity streamline plots were obtained using ANSYS CFD-Post.

Table 3.2: RPM test matrix for simulations

Propeller RPM	
Small (T-motor NS 22x6.6)	**Large Mejzlik 60x21**
1606	1000
2273	1400
2714	1800
3084	2200
3429	2600
3727	3000
3893	3400
4241	
4471	
5000	

3.1.1.4 Propeller geometric model

While the Computer-Aided Design (CAD) model of the propeller for the Mejzlik propeller was given for testing in simulation by the manufacturer, it was not available for the T-motor propeller in the same manner. Thus, it was scanned as a 3D point cloud and reconstructed in SolidWorks based on estimated airfoil profile sketches from the point cloud. The scanning was carried out using a Hexagon Metrology scanner HP-L-8.9 mounted on a Romer Absolute 7535 arm. This equipment can be seen in fig. 3.7.

Using the 3D point cloud scan visualised in fig. 3.8a, the propeller CAD model seen in figure 3.8b was obtained. It was exported to a parasolid file before being used for simulation in CFX. Both clockwise (CW) and counter-clockwise (CCW) propeller models were generated from the same scan, and simply mirrored to obtain the opposing orientation.

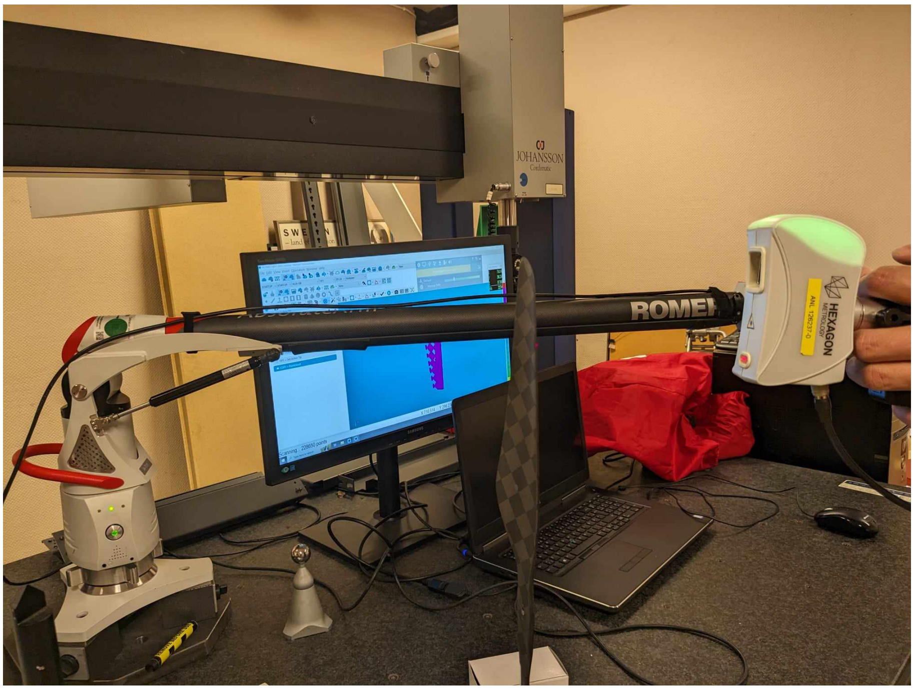

Figure 3.7: Propeller 3D scanning equipment and setup

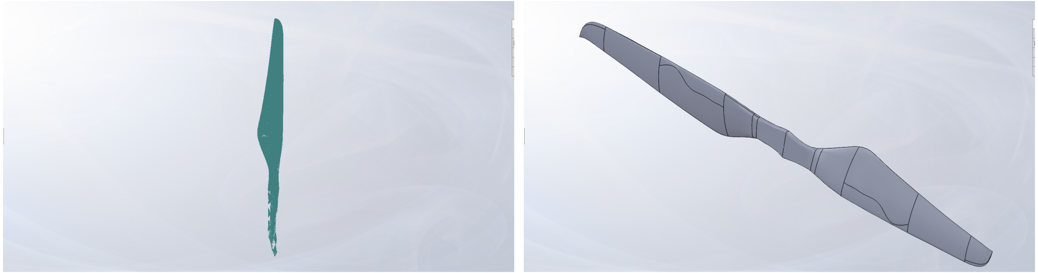

(a) 3D Point cloud scan of propeller **(b)** Scanned propeller CAD model

Figure 3.8: Computer models of scanned T-Motor propeller

3.2 Experimental Data

Due to the lack of available experimental data for coaxial propellers, and to help validate the simulation methodology, a test rig was set up to collect thrust data for coaxial simulations using the T-Motor propellers, and as part of the larger AMES project.

The experimental setup for the coaxial test of the T-motor NS 22x6.6 can be seen here represented in fig. 3.9. The thrust was measured using a manually calibrated single axis load cell (Vishay Tedea Model 1042 [26] read using a GW Instek GDM-8341 with 0.02% error [27]) in the z-direction, while an oscilloscope ([28]) was used to measure current and voltage draw, using the motor diagnostic cables to read the frequency signal and calibrating it to RPM. The propellers were individually powered by a T-Motor MN505S_KV320 motor, both powered by a 6S Lithium-Polymer (LiPo) battery. In order to keep overheating issues from affecting the test, the motors were allowed to cool and inspected using a thermal camera before carrying out the next test point in the matrix.

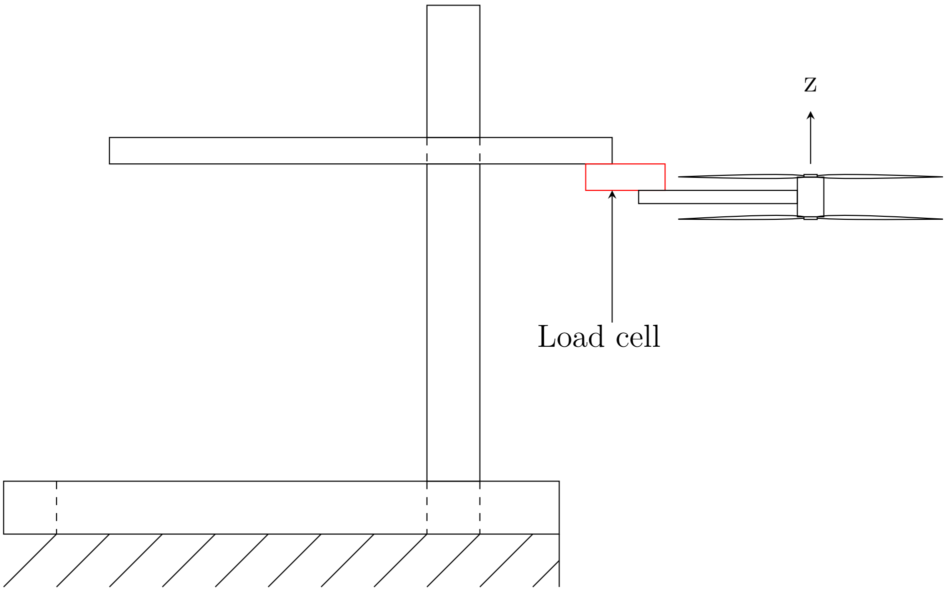

Figure 3.9: Coaxial configuration experimental setup

The propellers were hanging over a ledge in order to keep out of ground effect and get a better idea of the thrust generated in hover conditions. However, the test area is not completely free of obstructions, as seen in figure 3.10. This is somewhat closer to the environments the full-sized drone would be operating in, but does not properly match the simulation conditions.

Figure 3.10: Coaxial configuration experimental setup

4

Results and Discussion

The results obtained from the simulations and experiments and simulations are presented here, and their implications discussed. Pressure, velocity and vector plots from the simulations were obtained for all RPMs simulated, but to maintain brevity, and because many of them look very similar, the plots for only one RPM value for each propeller model are presented in the report. The raw data obtained is located in the appendices, and only the resultant plots of the data are found in this chapter for similar reasons.

Due to time limitations, a very brief investigation of a shroud around coaxial propellers was conducted, and the limited results are presented.

4.1 Grid independence study

The results of the grid independence study, conducted using the T-motor propeller geometry, can be seen in table 4.1. The second line with a fine propeller mesh changed the exit boundary condition to have a high turbulence opening, and that is not reflected in the mesh numbers.

Table 4.1: Results of grid independence study

Mesh	Elements		Thrust [N]	% thrust diff. from ind. data	% diff. change
	Domain	Propeller			
default	4513	1500579	38.129	14.220	-
coarse	24108	1500579	38.173	14.121	0.0990
fine	186057	1500579	38.267	13.908	0.2131
finer	1458852	1500579	38.411	13.585	0.3226
very fine	8955797	1500579	38.498	13.388	0.1975
superfine	57064915	1500579	38.514	13.352	0.0353
improved	8955797	1864793	35.051	21.145	-7.7570
fine	8955797	12042299	35.855	19.336	1.8090
fine*	8955797	12042299	35.855	19.335	0.00068
very fine	8955797	62479005	34.831	21.640	-2.3040

*High turbulence outlet

Based on the results of the grid independence study, a very fine domain mesh and a fine mesh with a high turbulence outlet were selected to conduct the rest of the investigation. The element quantities were approximately targeted when creating the grid for the coaxial domains, for both propeller models, and for the single propeller domains for the Mejzlik propeller, adn the shrouded propeller. The resultant mesh near the propeller can be seen here in figure 4.1. The grid selection criterion was based on the change in difference of the simulated thrust values from the independent experiment thrust values.

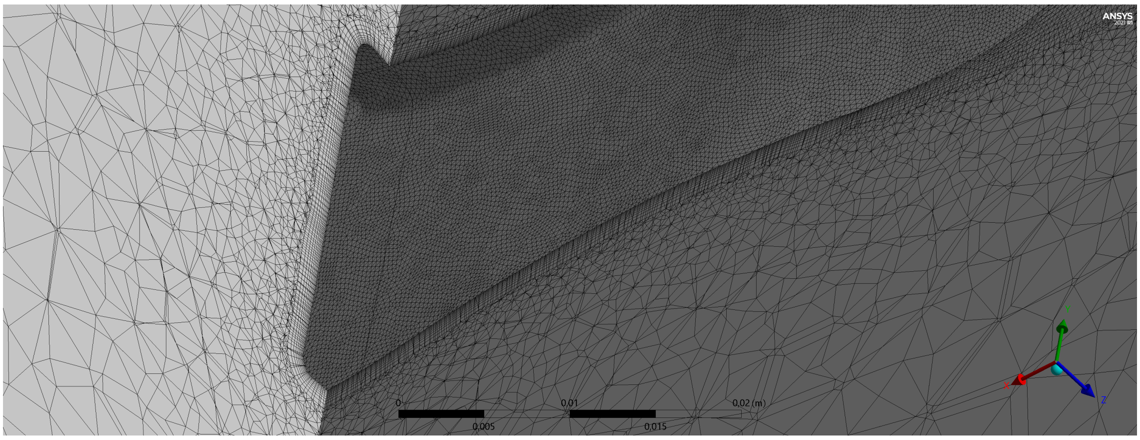

Figure 4.1: Visualisation of chosen mesh

4.2 Single propeller Validation

Following the grid study, results were obtained for a single propeller configuration and compared to experimental data provided by the manufacturers and independent data where available, as previously mentioned. The resultant plots for thrust, torque and power can be seen in this section.

4.2.1 Thrust validation

In fig. 4.2, the thrust output of the T-motor propeller is plotted against RPM. The data on the left shows that the simulation data under-predicts the thrust compared to the experimental data. On closer inspection of the data, the difference in thrust was seen to be relatively consistent, so the average of the difference in thrust of each RPM simulated against the independent data and the simulation dataset multiplied by this average difference (1.17) to adjust it, and plotted on the right in fig. 4.2. As expected, the data is much more closely aligned to the independent data, and over-predicts the thrust data from T-motor by a small consistent amount. However, since this adjustment is not rigorously defined, it is of dubious value for coaxial simulations unless it can be experimentally verified.

A similar comparison for the Mejzlik propeller was done against manufacturer provided data, and the results can be seen in fig. 4.3. This time, the simulation data aligns much closer to the manufacturer provided performance data. This helps verify that the simulation setup is accurate enough to predict real performance. The extrapolated data is plotted in a different colour, as noted in the legend.

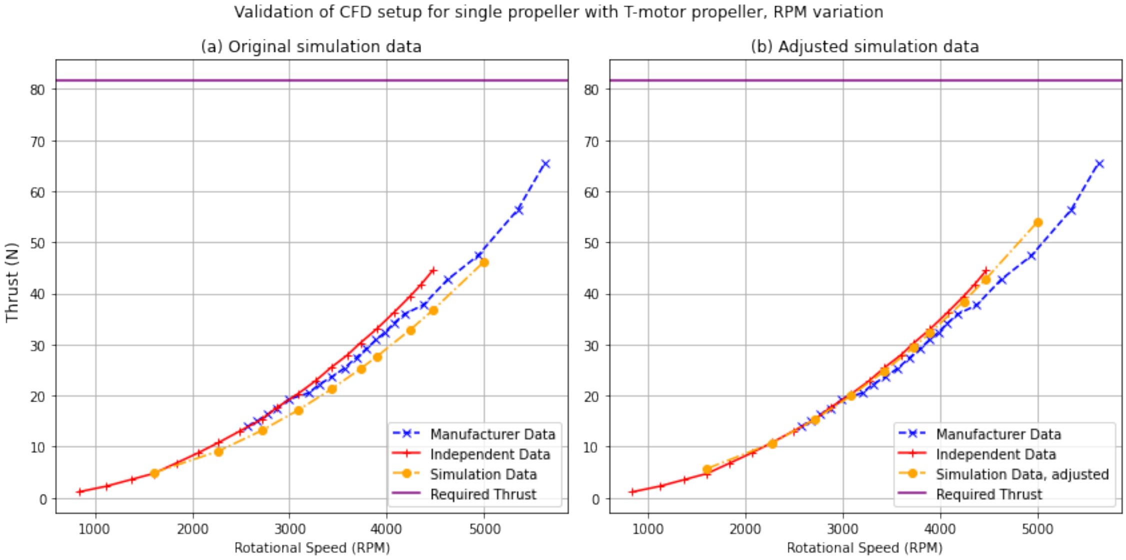

Figure 4.2: Validation of thrust for T-motor propeller against RPM change

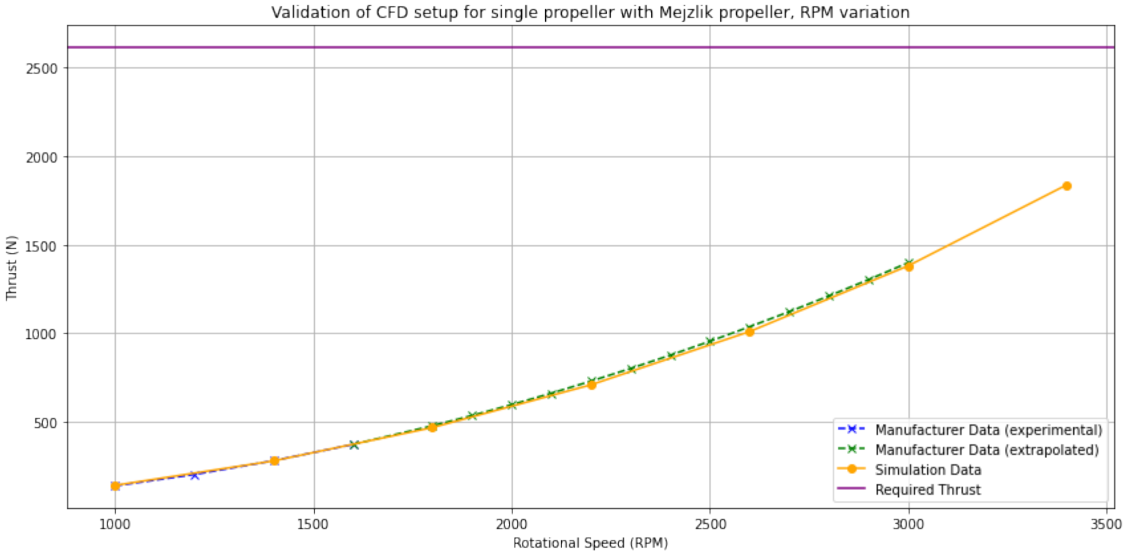

Figure 4.3: Validation of thrust for Mejzlik propeller against RPM change

In both plots, it can be seen that the single propeller does not produce the thrust requirement of a third of the total thrust to lift the drone in a hover configuration. This requirement is noted on the graph as the purple horizontal line.

Next, the torque required to obtain the thrusts seen in figures 4.2 and 4.3 were plotted. These plots can be seen in figures 4.4 and 4.5

Similar trends can be seen as for thrust, where the Mejzlik propellers closely match the manufacturer provided performance data, validating the simulation model, while the T-motor simulations need a similar adjustment to better match the experimental data. The adjustment factor for the torque (1.13) is different from the adjustment factor for the thrust.

The manufacturer data in both cases shows a higher thrust for the same torque,

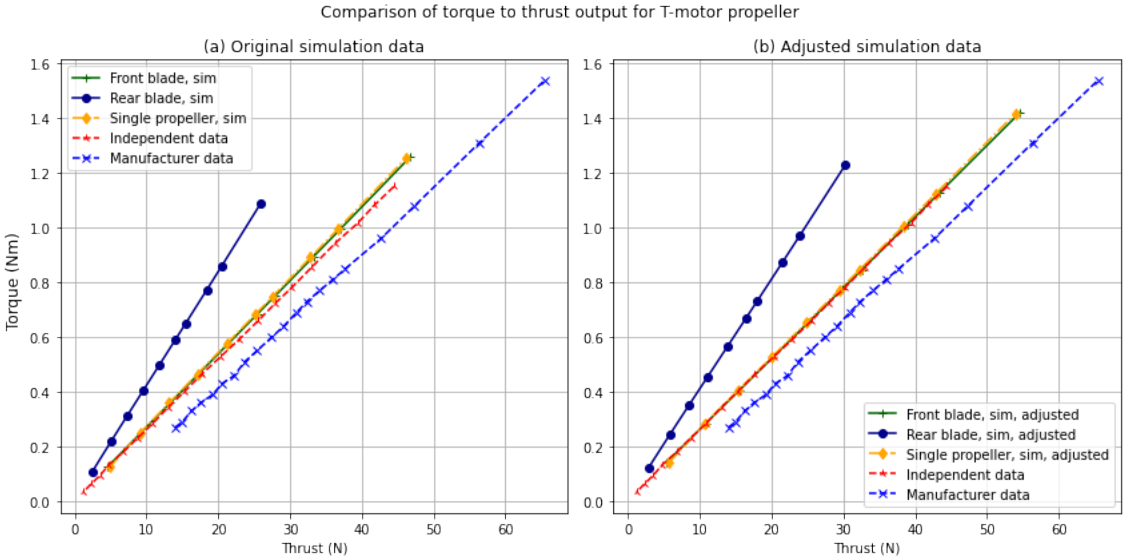

Figure 4.4: Validation of thrust for T-motor propeller against torque change

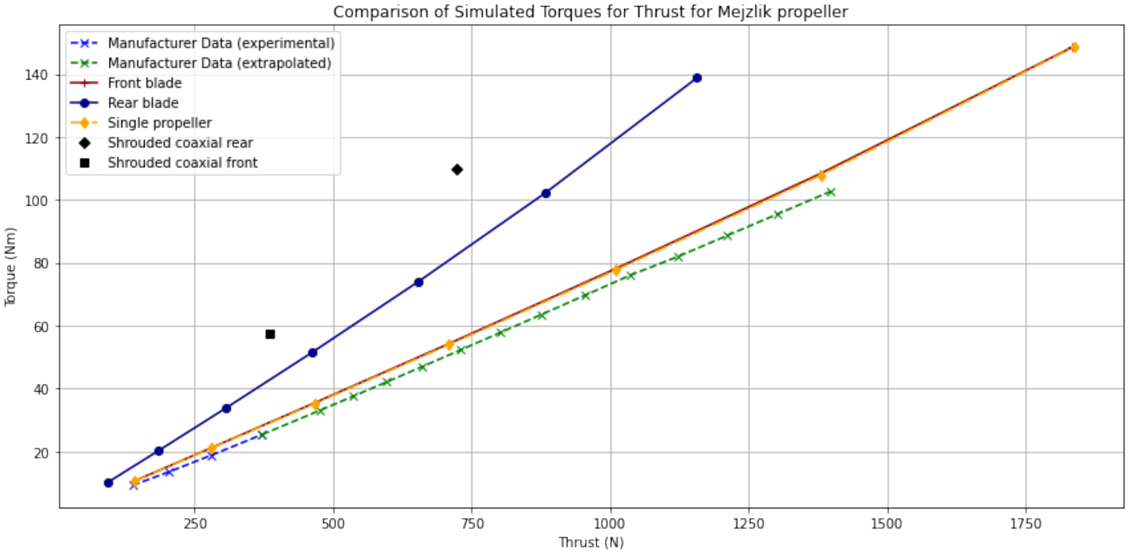

Figure 4.5: Validation of thrust for Mejzlik propeller against torque change

suggesting differences in the setup, that may represent conditions that may not occur frequently in real-world use.

The torque results from the coaxial simulations were also included in the plots, since there is not a total torque value, because the propellers spin in opposite directions and are powered independently. These results shows that the front rotor for both propeller models performs very similarly to a single rotor. The rear rotor in both cases requires higher torque to produce the same thrust, which makes sense, because the air has already been accelerated by the front propeller, and according to BEMT, the propeller will not accelerate the air to the same degree to produce an equal amount of thrust at the same rotational speed, since more energy needs to be put into the air - the energy required follows a quadratic relation to the speed of the air

[29]. To produce more thrust requires a higher rotation rate, which would require more torque.

The two data points from the shrouded propeller show that the thrust generated from the propellers for a given torque is much lower than the non-shrouded propellers. The rear propeller outperforms the front propeller when both are shrouded, though both are outperformed by the unshrouded rear propeller.

For the final single propeller validation, the power required to produce a given amount of thrust is plotted. Since the mechanical power is a function of the torque, it is not measured, but derived from the simulation data. In addition, the electrical power input will be higher than the mechanical power due to inevitable losses in conversion and transmission. The simulation was not configured for electrical power, so that aspect was not explored, and can vary highly based on the power setup of the testing equipment in experiment.

The results for power can be seen in figures 4.6 and 4.7.

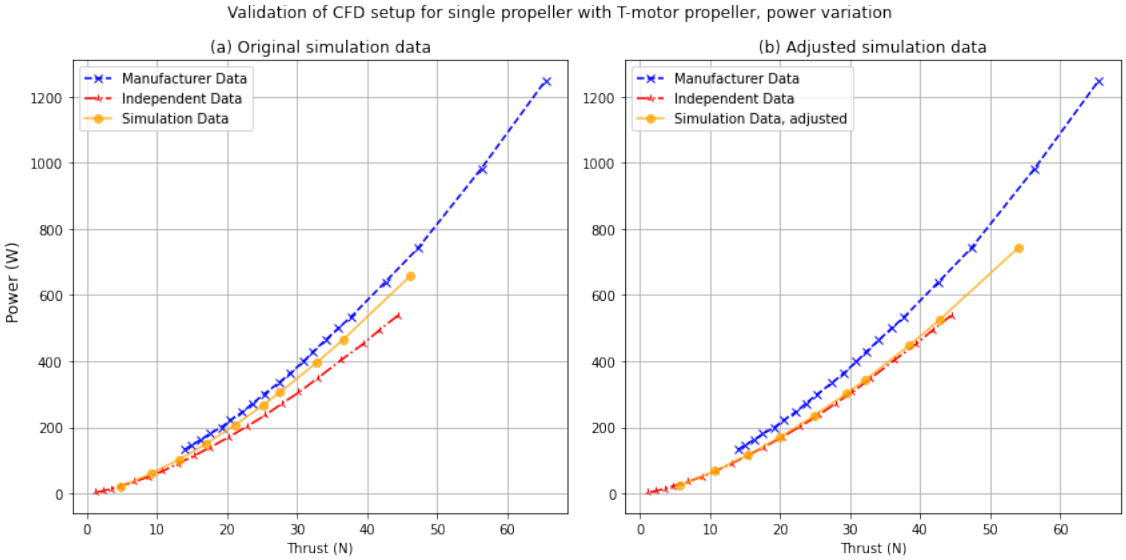

Figure 4.6: Validation of thrust for T-motor propeller against power change

The power to thrust comparison shows differences between the T-motor and Mejzlik propellers, as the manufacturer data for T-motor shows that it requires more power than independent testing and simulations show, but the reverse is seen for the Mejzlik propeller, as less power is required for the same thrust, again likely due to idealised test conditions.

Not much can be concluded from the results for T-motor propeller though, because the T-motor data does not indicate whether the measured power is electrical or mechanical. But it is likely to be electrical, as the power losses seem to be consistent, and losses in conversion from electrical to mechanical are expected. The simulation power, after adjustment, aligns more closely with the mechanical power measured in independent tests, further adding to the likelihood of T-motor measured power being electrical.

The main difference for the T-motor and Mejzlik propellers used in the simulation are the CAD model. Where Mejzlik themselves provided the CAD model for

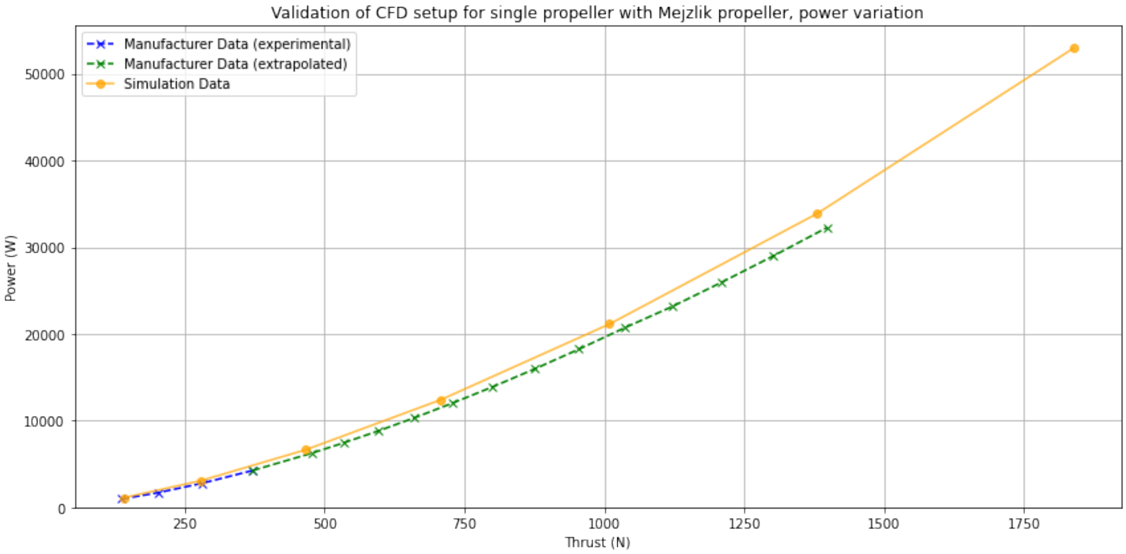

Figure 4.7: Validation of thrust for Mejzlik propeller against power change

numerical analysis, the T-motor model was scanned and modelled manually to approximate the geometry as closely as possible. This shows itself in the results as the Mejzlik propeller closely matches the manufacturer predicted thrust performance, but not the T-motor propeller before an adjustment is applied. This points strongly in favour of geometrical accuracy of the propeller model being the main issue in the simulations, but there could be other issues in the simulation that reduce the accuracy that are currently not being explored to reduce error.

4.2.2 Simulation plots

The velocity and pressure contour plots in the simulation need to be examined for coherency, to ensure that the numbers generated by the simulations are not flukes. The plots for the single propeller simulations for the highest available experimental RPM point are presented and discussed now.

4.2.2.1 Pressure Plots

To begin with, the pressure (static and total) contour plots for both propellers are presented, for the air in the domain, and on the propeller blade surfaces.

The pressure plots taken from a centre section of the domains, depicting both static and total pressure distributions show a region of low pressure in front of the propellers, and high pressures behind them, reaching the boundary of the domain. This shows that the propeller is drawing air from one direction and is pushing it out the other side, increasing the air pressure in the process, as expected of a propeller.

There are regions of low pressure in the pressure plots in the rotating domain behind the propeller, on the top and bottom of the domains. While these could the result of the tip vortices, the actual position of the propeller tips are offset 90° around the z axis from their position. The way the frozen rotor interface is implemented in ANSYS CFX could be the explanation for this low pressure cavity of air.

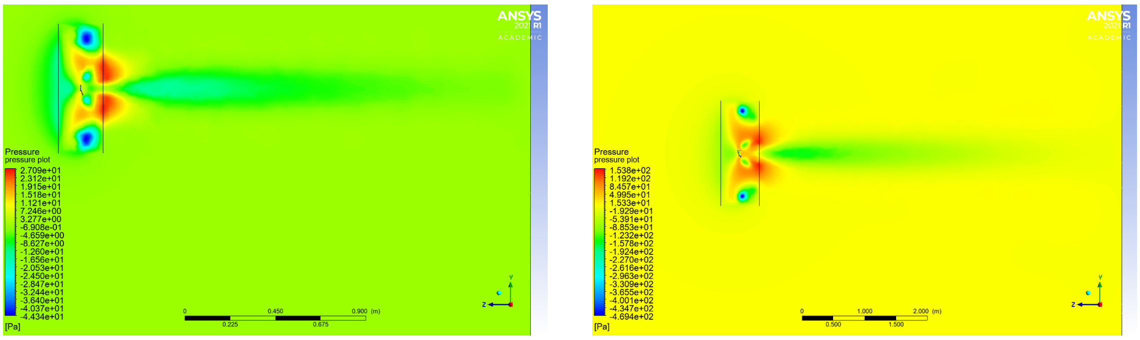

(a) T-Motor, domain pressure distribution

(b) Mejzlik, domain pressure distribution

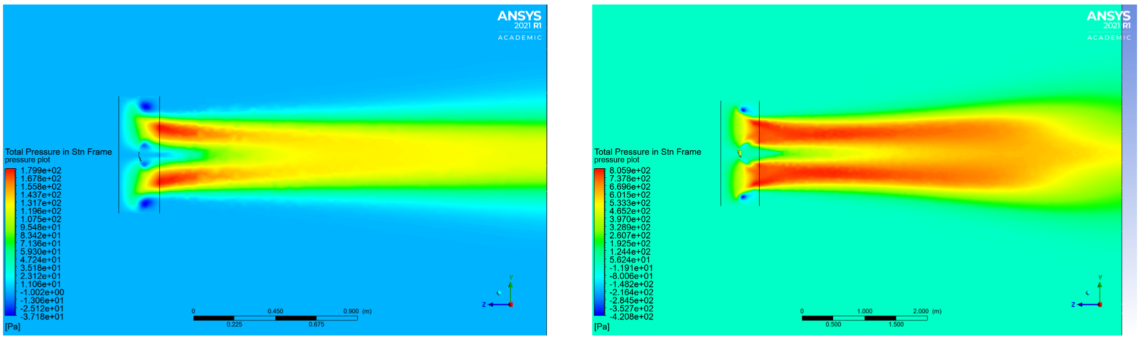

(c) T-Motor, domain total pressure distribution

(d) Mejzlik, domain total pressure distribution

Figure 4.8: Domain pressure plots

From the centres of the propellers, a jet of high pressure air is seen. This is more pronounced in the total pressure plot, and indicates that the majority of the air is pushed out behind the propeller disk, and would be responsible for generating thrust, due to the relative lower pressure at the front of the disk. The Mejzlik propeller shows a fanning out of the total pressure near the edge of the domain, and this is seen to a lesser extent for the T-motor propeller.
Next, the pressure distributions around sections of the propellers' spans are shown, showing the airfoil pressure distributions.

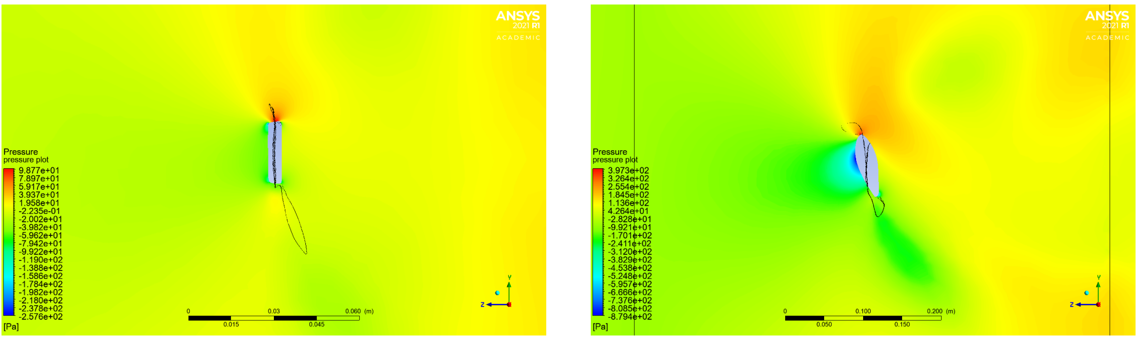

(a) T-Motor, 10% radius section pressure distribution

(b) Mejzlik, 10% radius section pressure distribution

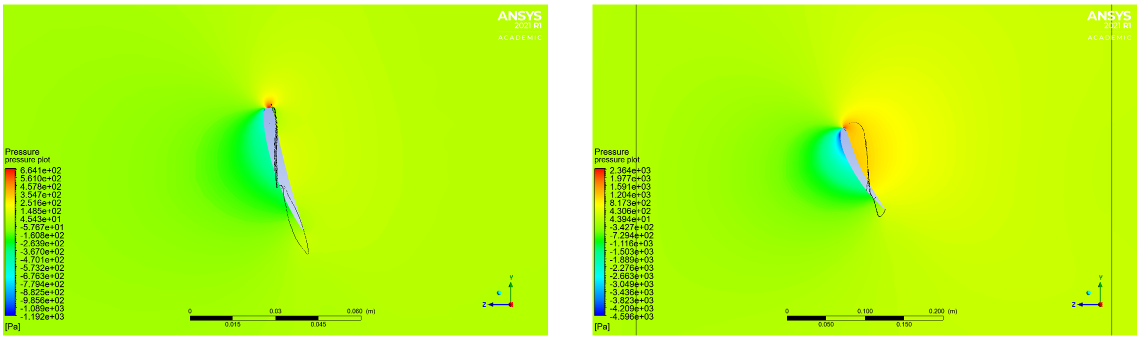

(c) T-Motor, 25% radius section pressure distribution

(d) Mejzlik, 25% radius section pressure distribution

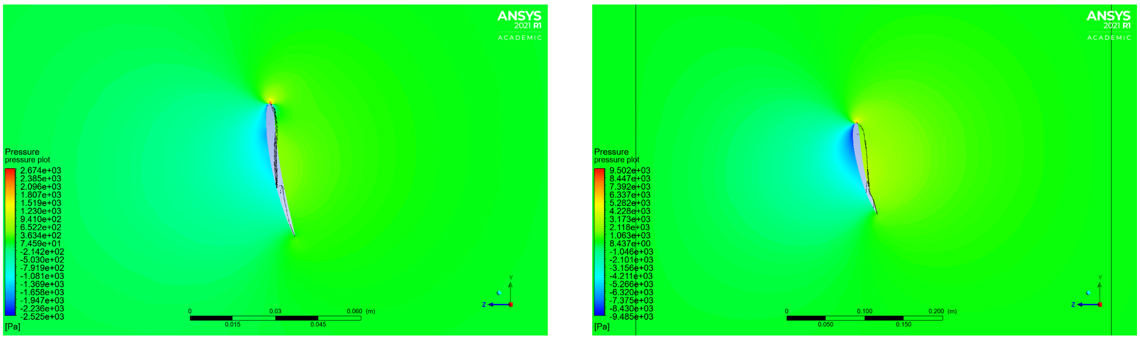

(e) T-Motor, 50% radius section pressure distribution

(f) Mejzlik, 50% radius section pressure distribution

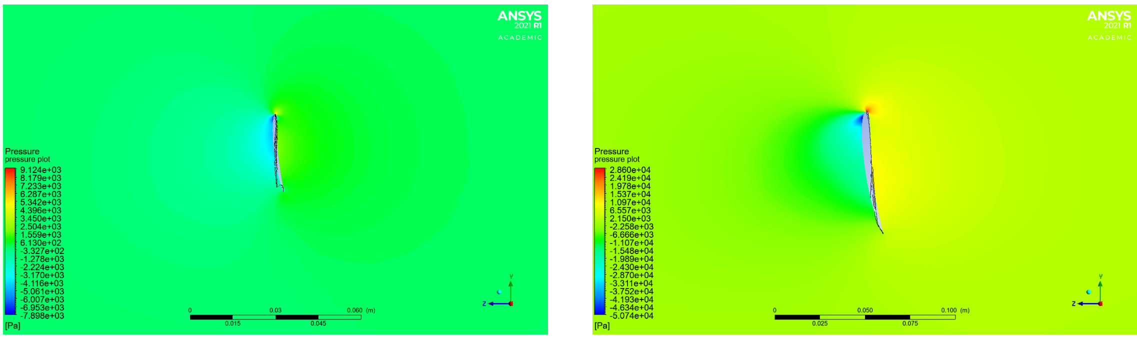

(g) T-Motor, 90% radius section pressure distribution

(h) Mejzlik, 90% radius section pressure distribution

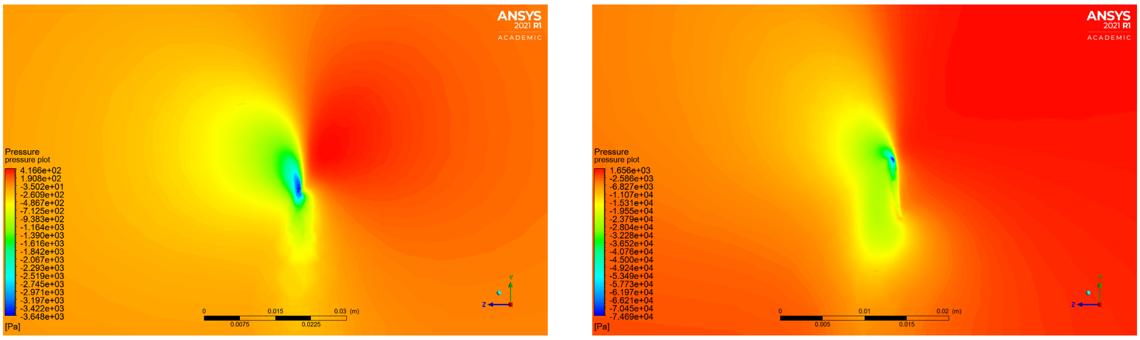

(i) T-Motor, 100% radius section pressure distribution

(j) Mejzlik, 100% radius section pressure distribution

Figure 4.9: Section pressure plots

The airfoil pressure distributions show low pressures on the airfoil facing incoming air, and relative higher pressure on the other side, as expected of an airfoil producing lift. This behaviour helps verify that the simulation is accurate. The high pressure region is more evident on the Mejzlik propeller. On both propellers, a high pressure region that shows the stagnation point on the airfoil is seen at the top, where the leading edge is. This helps verify that the propeller is rotating in the correct direction. The root of the Mejzlik propeller has a much higher angle of attack than at an equivalent section for the T-Motor propeller, and this results in the stagnation point moving further down the blade's leading edge.
At the tips of the propellers seen in plots 4.9i and 4.9j, a trailing vortex can be seen, fairly clearly for the T-motor model, and less so for the Mejzlik propeller. The Low pressure zone wraps around more of the airfoil at the tip than at other sections.
The pressure distribution over the airfoil surfaces, shown plotted in figure 4.10, show a similar distribution of pressures across the blade surface facing the oncoming air, and though difficult to see, a high pressure region on the leading edge of the blade, as expected, and further confirming the correct rotation direction of the propeller.

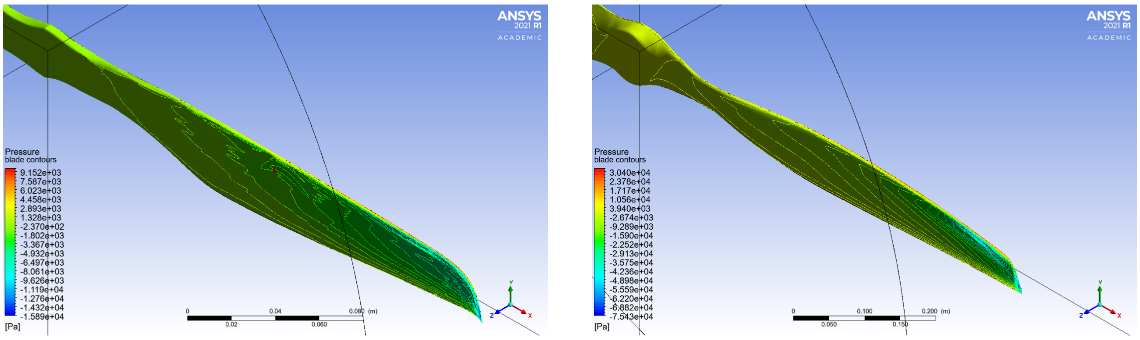

(a) T-Motor, blade pressure distribution front

(b) Mejzlik, blade pressure distribution front

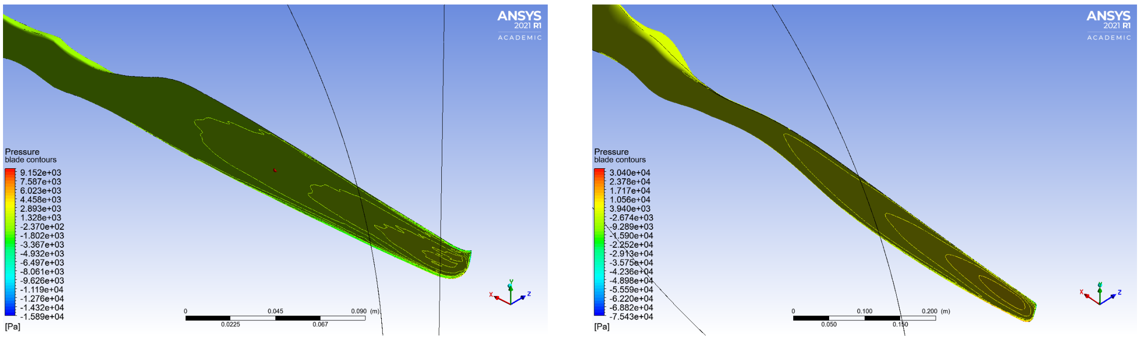

(c) T-Motor, blade pressure distribution back

(d) Mejzlik, blade pressure distribution back

Figure 4.10: Blade pressure plots

4.2.2.2 Velocity plots

Taking a look at the velocity plots in the stationary frame, for overall velocity and velocity along the z axis, denoted by frame w, shows a very similar distribution to

the total pressure plots, with low velocity air in front of the propeller accelerated in a jet behind the propeller. The T-motor propeller has a strong straight core jet all the way to the boundary, while the Mejzlik propeller decelerates before the boundary. This may be an artifact of the way the domain size is defined, and the same behaviour might be seen with a larger simulation domain for the smaller propeller.
The exit velocities also show stratification as the exhaust spreads out, along the radius of the propeller. This suggests that most of the acceleration of air happens at the centre of the propeller disk and less near the tips. Since the angle of attack is higher near the root of the propeller, as seen in figures 4.9c and 4.9d, this part of the propeller does more work on the air flowing past than at the tips, even though the tips are moving through the air faster.

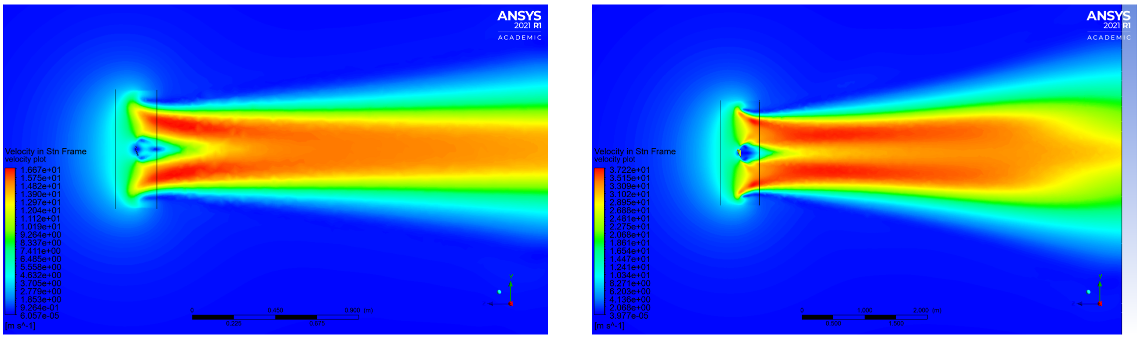

(a) T-Motor, domain velocity in stationary frame

(b) Mejzlik, domain velocity in stationary frame

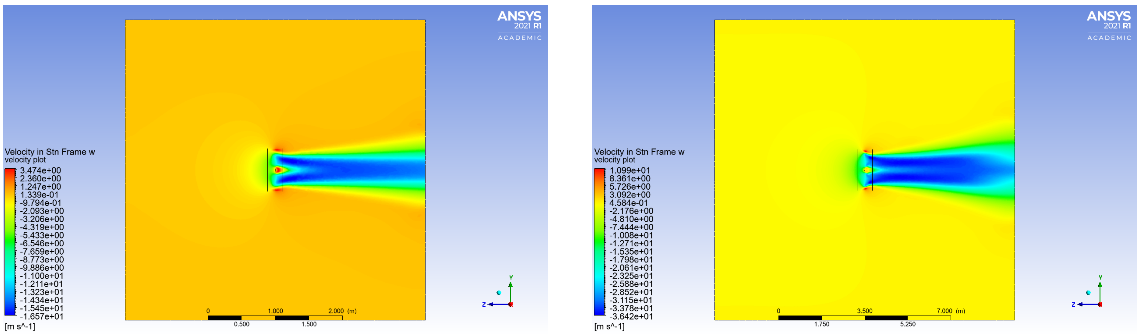

(c) T-Motor, domain velocity in stationary frame w

(d) Mejzlik, domain velocity in stationary frame w

Figure 4.11: Domain stationary frame velocity plots

The velocity streamline plot in fig. 4.12 shows the swirl induced by the propellers into the air, and the gathering of air from the front into a thrust-generating jet behind it.
The swirl induced into the airflow is much more evident for the larger Mejzlik propeller than for the T-motor propeller, from the larger torque imparted to the air from the propeller.
Based on the results for the single propeller configuration, the methodology used for the simulations appears robust enough to be extended to the coaxial propeller simulations, whose results are presented and discussed in the next section. Since the

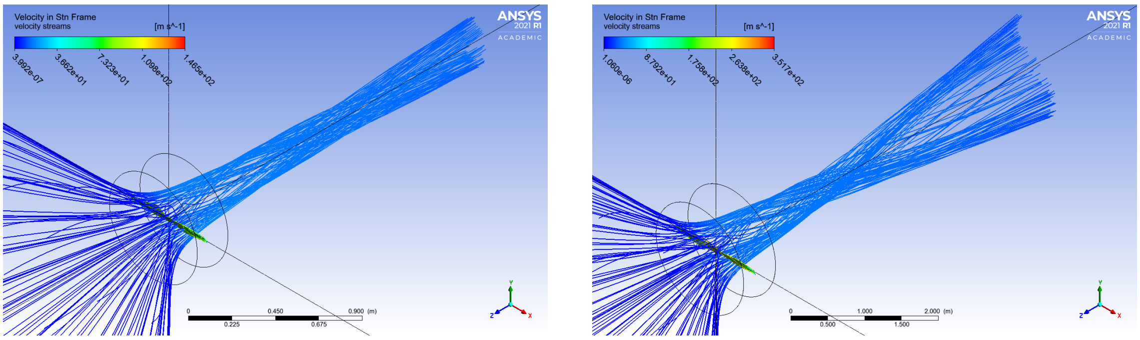

(a) T-Motor, domain velocity in stationary frame

(b) Mejzlik, domain velocity in stationary frame

Figure 4.12: Velocity streamline plots

adjusted values more closely match the experimental data, they will be used going forward for the analysis.

4.3 Coaxial Thrust Simulation Results

4.3.1 Thrust Generation

The simulations show that the coaxial configurations produce the required amount of thrust at the highest RPM tested. This can be seen in fig. 4.13

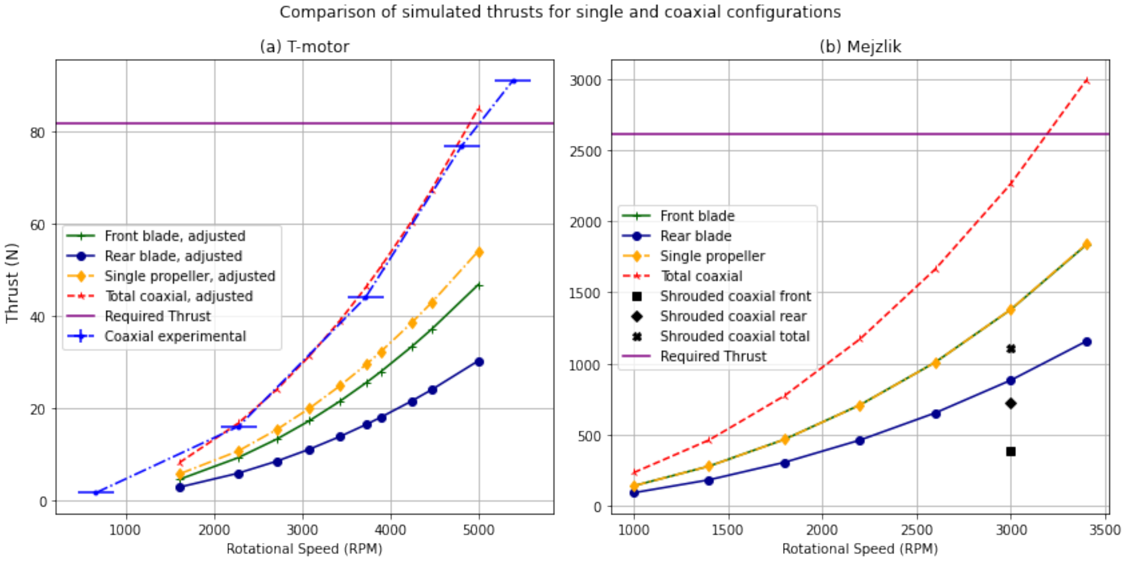

Figure 4.13: Coaxial thrust production

The T-motor propeller simulations show some over-prediction of thrust compared to the experimental data collected, and this is likely due to the motor arm not being included in the simulation, as well as the confined space of the experimental testing area. The simulation was assumed to be in a large unimpeded space, which allows for unobstructed airflow in the domain. However, the simulation mostly aligns with

the data collected, and this helps validate the simulation methodology for coaxial rotors, as well as the adjustment factor, though more data would be ideal.
The atmospheric conditions during experimental testing were found to be 99.354 kPa and 27.74 °C, which, from the equation of state 2.4 would make the air less dense than standard sea-level atmospheric conditions, allowing the propeller to perform with lower drag than the simulation conditions by a small amount, while also being affected by environmental obstructions as noted in the methods.
The single propeller simulation also seems to produce more thrust than the front rotor for the smaller T-motor propeller. The cause of this is uncertain, but the main difference from the Mejzlik propeller is in the rotor spacing, and geometrical accuracy of the propeller blades - these could well be the cause of the discrepancy.
The Mejzlik propeller does not show anything notable. There seems to be no change in thrust generation between a single propeller configuration and the front propeller, but the rear propeller must work with already accelerated air, and thus produces less thrust for the same rotational speed, as discussed before in section 4.2.1.
The highest thrust in experimental data for the T-motor propeller was obtained at the maximum possible power to the motor used for testing. According to T-motor, the propeller is capable of producing even more thrust [30], but the motor used was not capable of reaching that level of performance for the propeller.
Again, the shrouded propellers are very badly underperperforming, with the total thrust generated by a shrouded coaxial pair is higher than the rear propeller at the same RPM. The front propeller generates less thrust than the rear propeller again.
Next, the mechanical power of the simulated coaxial systems is compared to the individual rotors. This is seen in figure 4.14.

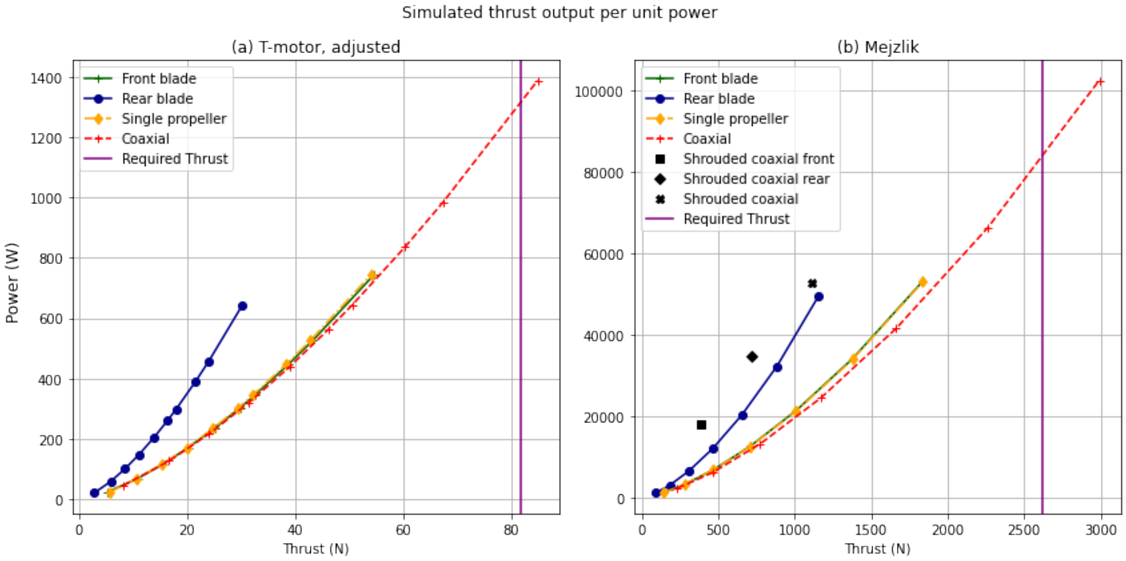

Figure 4.14: Coaxial power required per unit thrust

The power required for the T-motor propeller in a coaxial setup remains very close to that required for a single propeller, and only begins diverging at higher RPM values, when higher thrust is generated. The data for the Mejzlik propeller shows a similar trend, where the power required starts diverging with higher thrust generation.

This suggests a strong relationship between thrust and power. There is no explicit relationship defined, but there is a relationship between power and torque. The thrust and RPM relationship depends strongly on the airfoil characteristics of the propeller, while the power-thrust would also have to account for the efficiency of the propulsion system driving the propeller, which could vary widely, making it difficult to derive a universally applicable empirical relation. This does hint that coaxial configurations are more power efficient at higher thrust values.

As expected, for both propeller models, the rear propeller requires more power to produce the same thrust as the front propeller or a single propeller, having to work with already energised air from the front propeller, while the single propeller and front propeller have very similar thrust-power profiles. The overall efficiency of the system is higher than a single propeller, since a single propeller must either be larger or spin much faster to produce an equivalent thrust, and both require higher power draw, especially to spin faster, since the power required appears to follow a power law. While the rear propeller accelerates the air less than the front propeller for the same input, it requires less power than a single equivalent propeller for the same overall acceleration of the air by the two propellers.

While it has been observed that the total thrust produced by the shrouded coaxial propeller is higher than that for the rear propeller for the test point, it does so using more power than the rear unshrouded propeller. The front propeller is once again shown to be worse performing than the rear propeller when both are enclosed in a shroud.

It has been observed several times that the rear propeller produces less thrust than the front propeller, all inputs being equal. As discussed in the theory section, this reduction in the thrust caused by the front rotor can be quantified using the interference factor k_{int}. A plot of the interference factor can be seen in fig. 4.15.

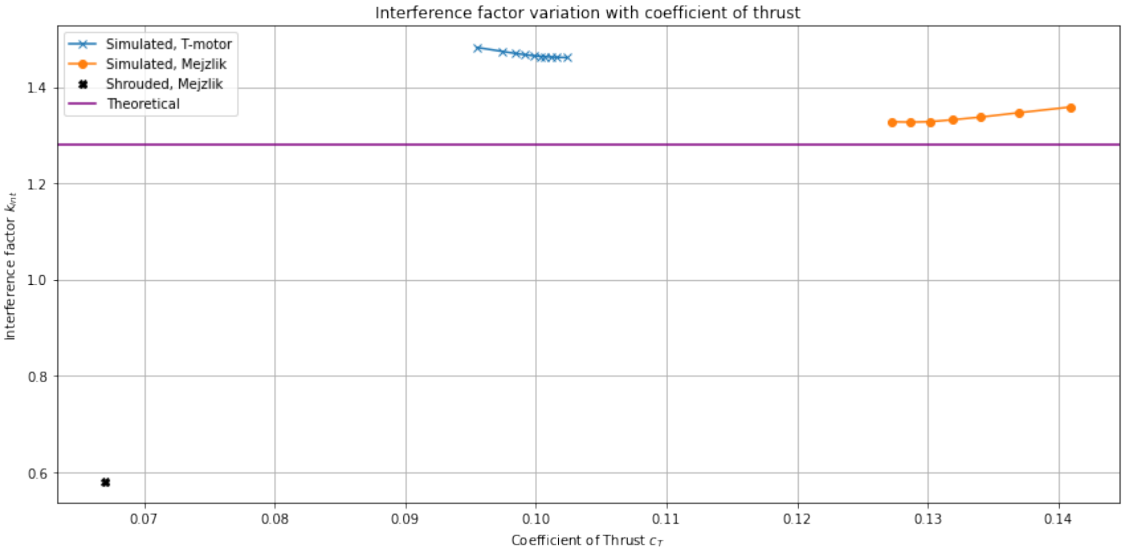

Figure 4.15: Interference factor

According to the theory, an ideal interference factor is 1.281 [20], but as seen in the plot, both simulations have a higher value than that. The T-motor factors are in general higher than those for the Mejzlik propeller. Since they are both higher than the theoretical value, it is not simply an issue of the differences in geometry, but also of the simulation setup. The theory also assumes ideal conditions, so to verify which value is more realistic, experimental results will have to be obtained for the coaxial propeller configuration beyond what was gathered to make any definitive statements.

The shrouded case shows a lower interference factor than the ideal theoretical value, implying better coaxial performance. However, this is due to the formulation of the interference factor, which includes the ratio of the top propeller thrust to the bottom propeller thrust twice, as seen in equation 2.15.

4.3.2 Simulation plots

Looking at the contour plots for the coaxial simulation can yield insights into the validity of the simulation, as well as possible explanations for unexpected phenomena.

4.3.2.1 Pressure plots

As with the single propeller simulations, the pressure (static and total) plots for both propellers are presented, both in the domain, and on the propeller surface, to begin with.

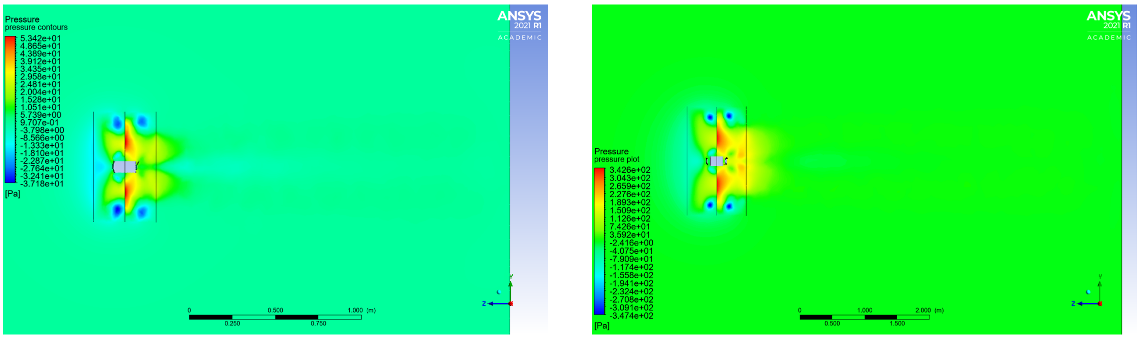

(a) T-Motor, coaxial domain pressure distribution

(b) Mejzlik, coaxial domain pressure distribution

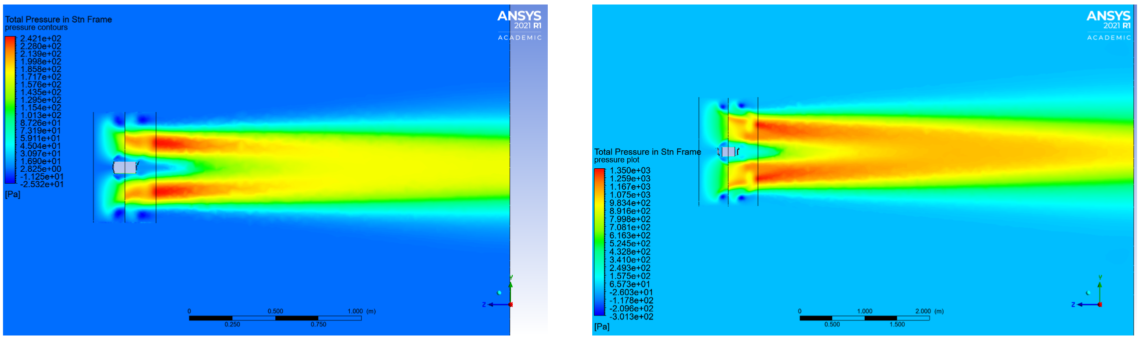

(c) T-Motor, coaxial domain total pressure distribution

(d) Mejzlik, coaxial domain total pressure distribution

Figure 4.16: Domain pressure plots for coaxial simulations

The pressure distributions behind the propellers look very similar to those seen for the single propeller simulations. The interface between the two rotating domains shows a discontinuity, especially in static pressure. This may be due to the mixing planes interface implemented between the two domains in the setup, that circumferentially averages the conditions across the interface, as explained in section 2.1.5.2. The static pressure jet behind the center of the disk appears much weaker here than for the single propeller simulations, and this is likely a result of swirl reduction by the second propeller rotating in the opposite direction.
The plots for the static pressure distribution around the airfoil sections do not show any notable irregularities compared to the single propeller simulations, and confirm that the propellers are rotating in opposite directions in the simulation from the stagnation points at leading edge at each section. The rear propeller also shows smaller pressure distributions than the front one, matching the lower thrust seen previously in figure 4.13. There is no motor representation void for the Mejzlik propeller at 10% of the propeller span, because of the much larger overall radius.

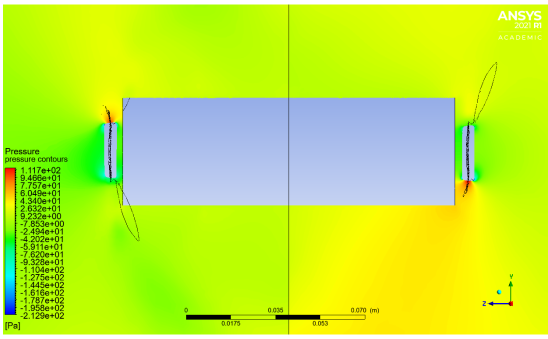

(a) T-Motor, 10% radius section pressure distribution

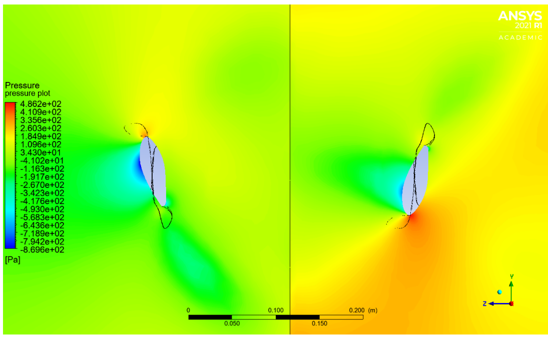

(b) Mejzlik, 10% radius section pressure distribution

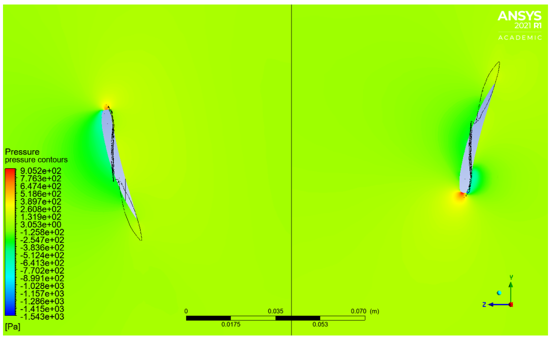

(c) T-Motor, 25% radius section pressure distribution

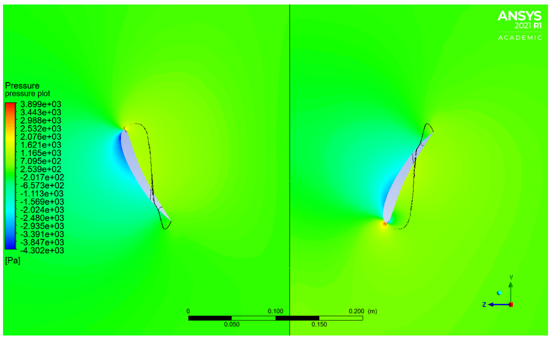

(d) Mejzlik, 25% radius section pressure distribution

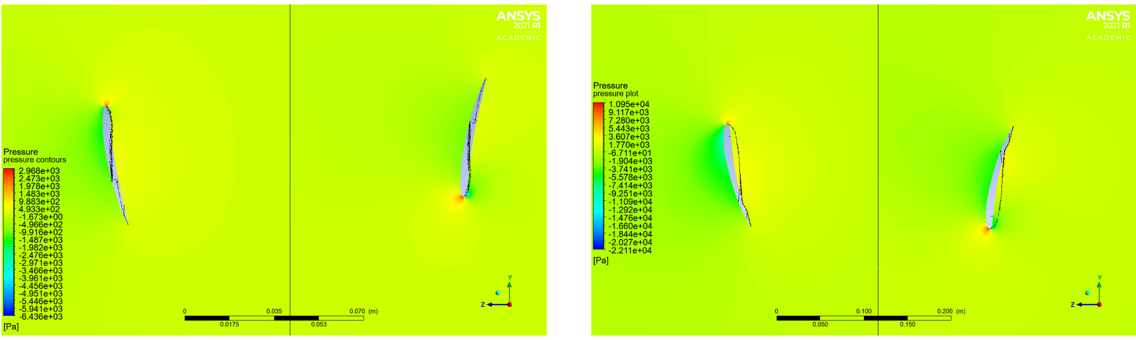

(e) T-Motor, 50% radius section pressure distribution

(f) Mejzlik, 50% radius section pressure distribution

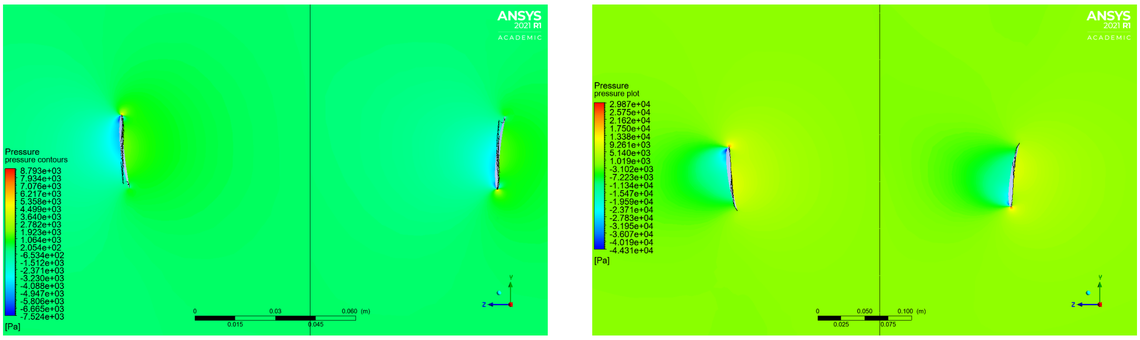

(g) T-Motor, 90% radius section pressure distribution

(h) Mejzlik, 90% radius section pressure distribution

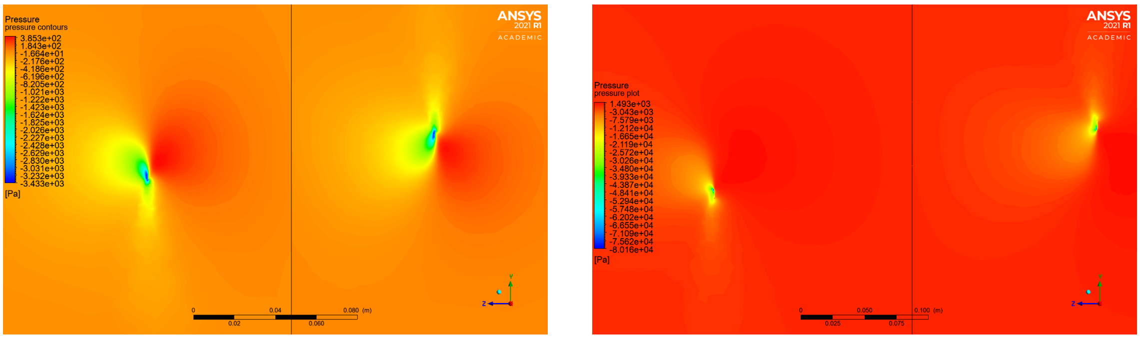

(i) T-Motor, 100% radius section pressure distribution

(j) Mejzlik, 100% radius section pressure distribution

Figure 4.17: Section coaxial pressure plots

Likewise, the blade pressure distribution plots look very similar to those seen for the single propellers seen in fig. 4.10
Here, the high pressures on the leading edges can be seen more clearly than for the single propeller plots, and it is easier to compare the section plots of pressure against the surface pressure plots. The pressure distribution is again as expected for an airfoil functioning correctly, with lower pressures on the surface facing away from the lift production direction relative to the opposite surface of the blade.

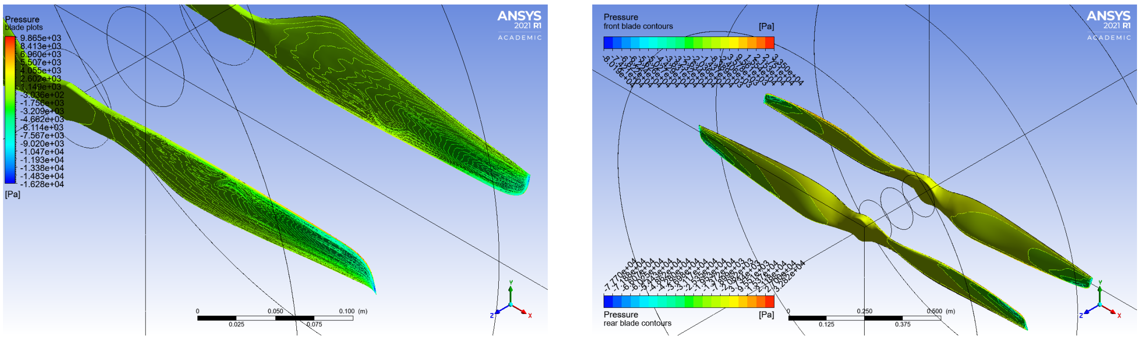

(a) T-Motor, coaxial blade pressure distribution front

(b) Mejzlik, coaxial blade pressure distribution front

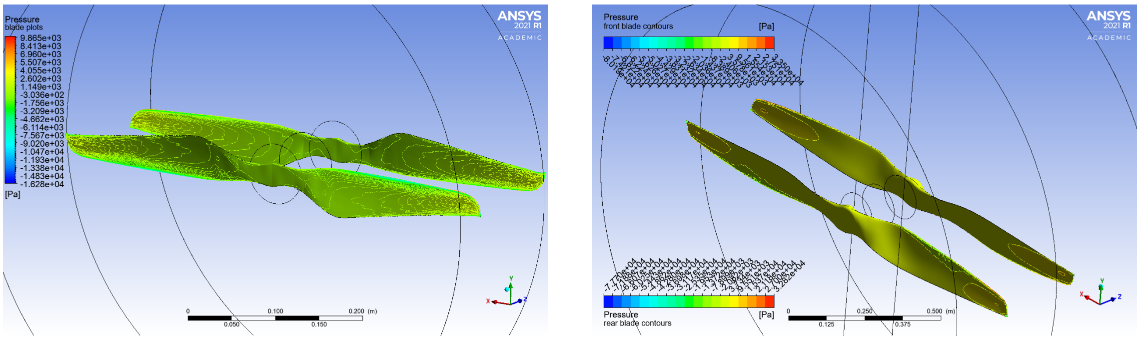

(c) T-Motor, coaxial blade pressure distribution back

(d) Mejzlik, coaxial blade pressure distribution back

Figure 4.18: Coaxial blade pressure plots

4.3.2.2 Velocity plots

The velocity plots again show similar results to the single propeller simulations, however, the exit velocity jet for the T-motor propeller appears more uniform than for the Mejzlik propeller. The reason is unknown, and cannot be explained by deswirling of the air by the rear propeller, since the plot for the Mejzlik propeller shows a stratified velocity distribution.

The velocity streamlines clearly show the swirling motion of the air behind the propellers has been reduced, due to the counter-rotation of the rear propeller, compared to the streamlines for the single propeller. The reduction of swirled air by counter-rotation allows recovery of some of the energy as thrust, increasing the system's efficiency.

The flow between the propellers can also provide some insight as to the changes in airfoil between between the propellers. The T-motor propeller seems to inherently generate more swirl that the Mejzlik propeller, this could be attributed to CAD model quality, especially at the hub region where most of the swirl is seen.

The air from the front propeller is seen to be directed to the hub region of the propeller, where the highest angle of attack is, allowing the rear propeller to work more effectively, even if the entire span is not loaded. Experiments with smaller potentially could possibly increase the system efficiency by allowing utilisation of the whole blade span, if an equal torque propeller is used, while retaining the torque

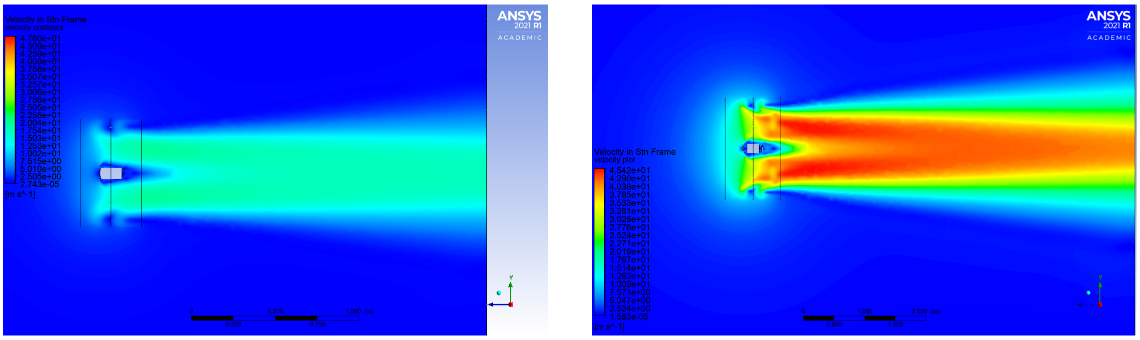

(a) T-Motor, coaxial domain velocity in stationary frame

(b) Mejzlik, coaxial domain velocity in stationary frame

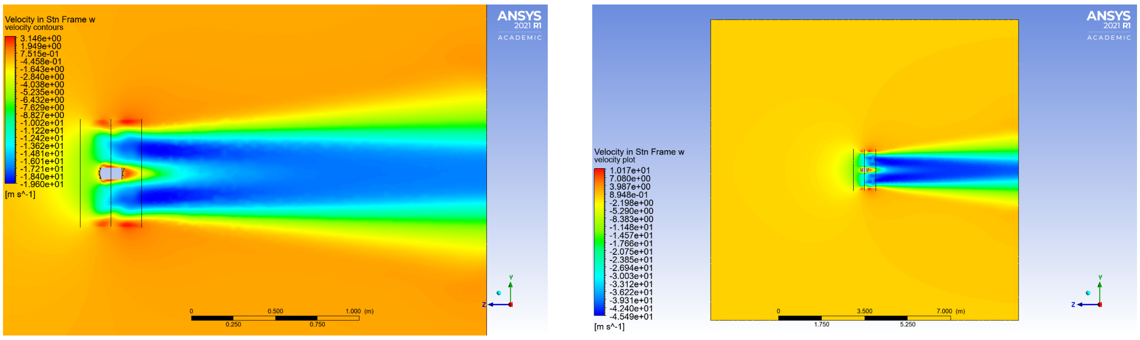

(c) T-Motor, coaxial domain velocity in stationary frame w

(d) Mejzlik, coaxial domain velocity in stationary frame w

Figure 4.19: Domain coaxial stationary frame velocity plots

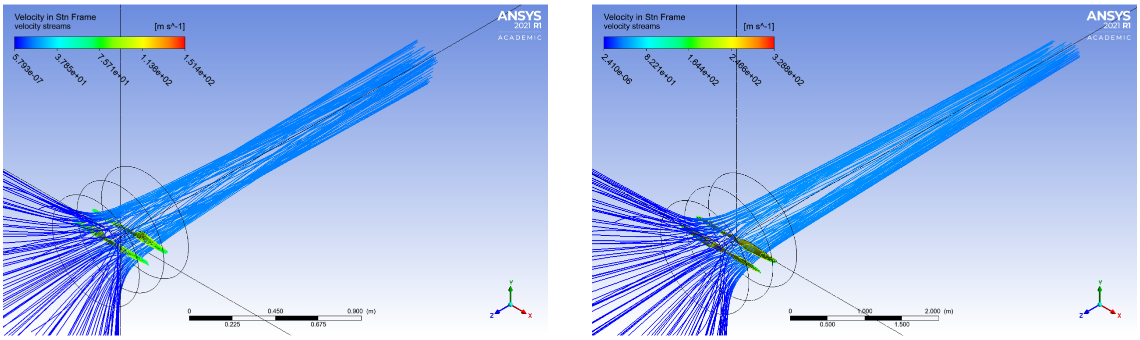

(a) T-Motor, coaxial domain velocity in stationary frame

(b) Mejzlik, coaxial domain velocity in stationary frame

Figure 4.20: Coaxial velocity streamline plots

reaction neutralisation advantage of a contra-rotating system and reducing weight. A higher pitch propeller may also work well in this regard.

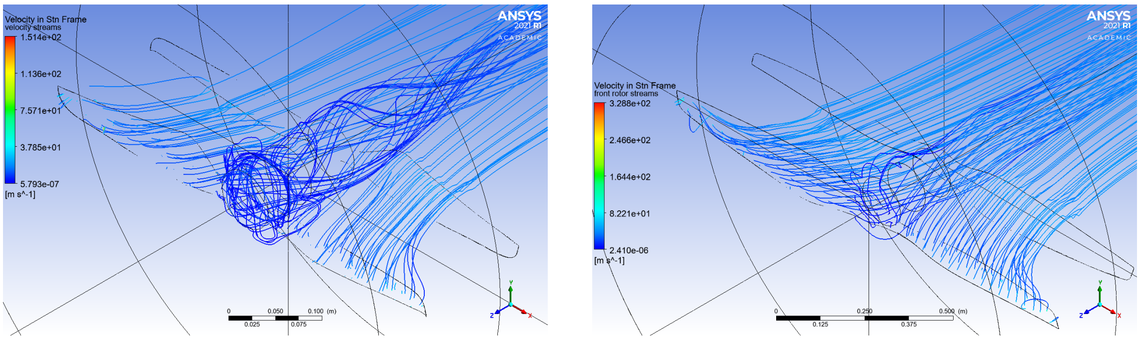

(a) T-Motor, coaxial domain velocity in stationary frame

(b) Mejzlik, coaxial domain velocity in stationary frame

Figure 4.21: Coaxial velocity streamline plots

4.3.3 Shrouded Coaxial Rotors

The shrouded coaxial propellers have shown very underwhelming performance compared to both an unshrouded single propeller and unducted coaxial propellers. A look at the pressure and velocity plots may provide an idea of why this is the case.

4.3.3.1 Pressure plots

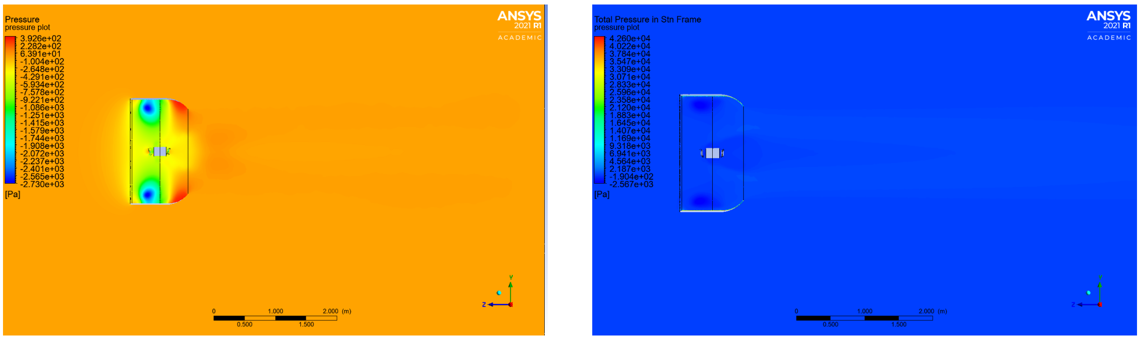

(a) Shrouded propellers, domain static pressure

(b) Shrouded propellers, domain total pressure in stationary frame

Figure 4.22: Shrouded propellers domain pressure plots

It is immediately apparent from the plots that the exhaust pressure from the shroud is not much higher than ambient pressure, both from the total and static pressure plots. The static pressure plots show that the inside walls of the converging section experience the highest pressure, but this not translate to high pressure of air being pushed behind the propeller. The total pressure plots also seem to show a buildup of pressure on the inside walls of the duct. This is better seen in fig. 4.23b, which is a zoom on the walls. The majority of the air is working to increase the pressure on the walls of the shroud rather than being accelerated out of the converging duct at the rear of the shroud.

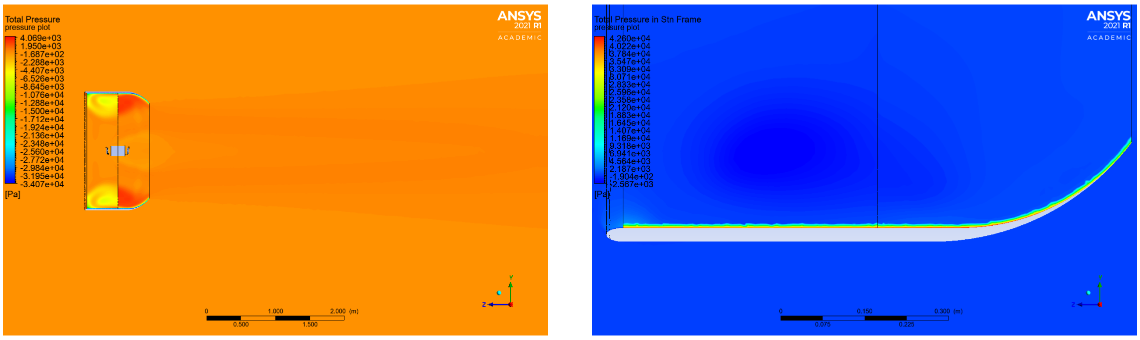

(a) Shrouded propellers, domain total pressure

(b) Total pressure distribution on shroud wall

Figure 4.23: Shrouded propellers domain pressure plots

The airfoil section pressure distributions show some differences from the coaxial airfoil section pressure plots, with the front propeller not having a clear suction side and pressure side in some sections along the blade span, as seen in subfigures 4.24b and 4.24d. This would be the cause of low thrust seen in figure 4.13. The rear propeller airfoil sections appear to function as designed, with a clear stagnation point, a pressure side and a suction side in all plotted sections except at the tip, where the vortices form from the low separation between the pressure and suction sides.

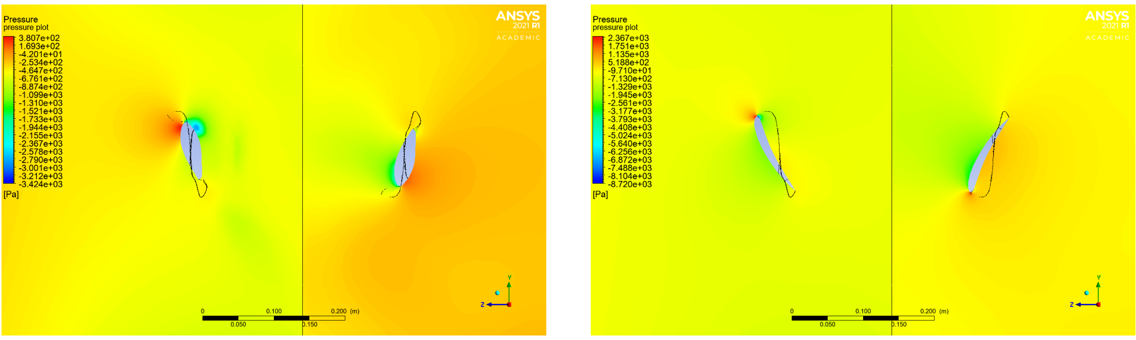

(a) Shroud, 10% radius section pressure distribution

(b) Shroud, 25% radius section pressure distribution

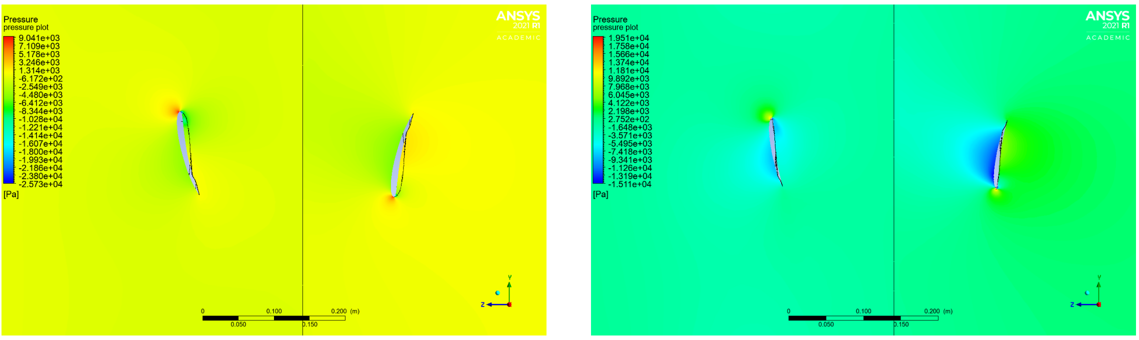

(c) Shroud, 50% radius section pressure distribution

(d) Shroud, 75% radius section pressure distribution

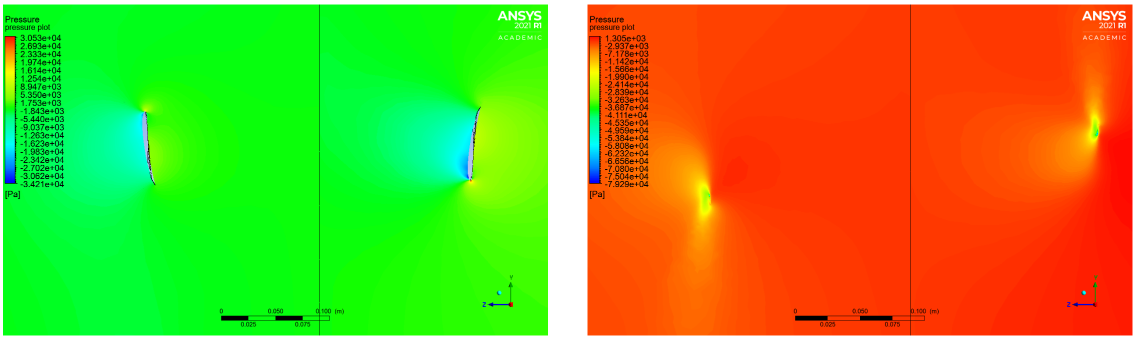

(e) Shroud, 90% radius section pressure distribution

(f) Shroud, 100% radius section pressure distribution

Figure 4.24: Shrouded airfoil section pressure plots

The blade surface pressure plots show a similar distribution of pressures on the pressure (rear) side of the front propeller blades, as there is a low pressure zone from the mid radius of the blade to the tip. The whole length of the front propeller blades are not being used to generate thrust, making it very inefficient compared to the unshrouded front propellers, as seen in the coaxial torque and power plots.

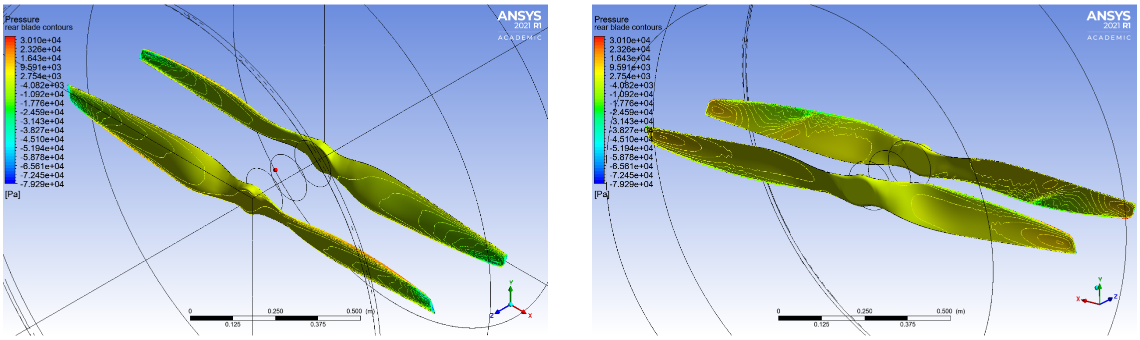

(a) Shrouded propellers, blade static pressure on front

(b) Shrouded propellers, blade static pressure on back

Figure 4.25: Shrouded propellers blade pressure plots

4.3.3.2 Velocity plots

Plotting the velocity may provide a better idea of what is happening to the air flow, since the increased pressure from the propellers is not being used to generate thrust as effectively as the unshrouded propellers.

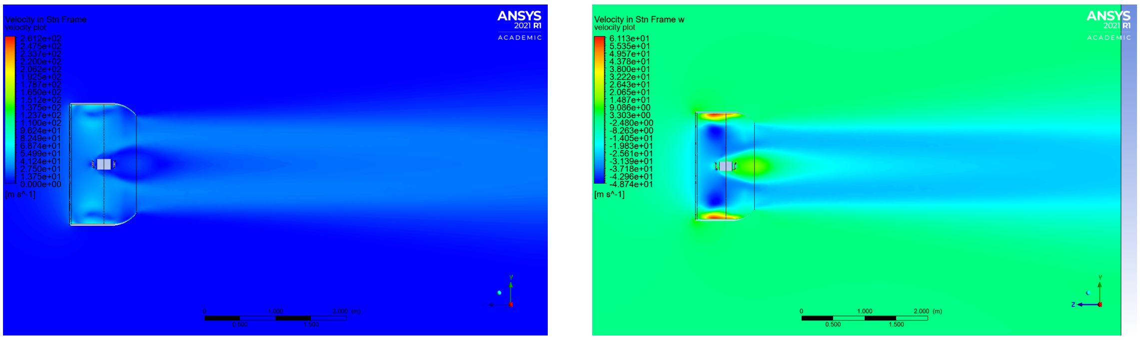

(a) Shrouded propellers, domain velocity in stationary frame

(b) Shrouded propellers, domain velocity in stationary frame w

Figure 4.26: Shrouded propellers domain velocity plots

The cause of low thrust can be immediately identified, as the air that should be accelerated out of the duct is instead sticking to the walls of the duct, as seen in figure 4.26b, creating a thick boundary layer between the propeller and the duct walls. The velocities plotted in 4.26b once again confirm that the air going out of the duct behind the propellers is not much different from ambient air, which is not the case with the unshrouded propellers, and the reason for the relative low thrust. The design of the duct is the likely culprit, as the propellers are not able to move the boundary layer sticking to the walls, and convert it to thrust, so a much smaller tip gap between duct walls and propeller tips may be the solution, similar to that employed in jet engines.

A plot of the velocity streamlines reveals that the air may be swirling near the tips, intensifying tip vortices that would otherwise dissipate into the ambient air. Gig. 4.27b shows that very little air makes its way to the rear propeller to be accelerated behind the duct.

The simulation plots obtained show how important duct design is, and that simple geometry without optimisation will actually decrease propeller performance in a duct. The duct's design is critical in preventing reduction of performance, and it may be the case that propellers designed for use in open air may be wholly unsuited to be used in ducts, but that is a conclusion that cannot be made from the results obtained for this report. More data will need to be compiled to make a definitive statement. Principles of turbomachinery design are likely to play an important role in combining propellers and ducts to maximise thrust generation, since jet engines, in very simple terms, are multiple rotors within a duct that generate thrust (and power) through their design. Of note is that rotor blades in jet engines are intended to work with pressure change rather than velocity, and due to the design philosophy of propellers, they may be inherently unsuited to being placed in ducts as designed here.

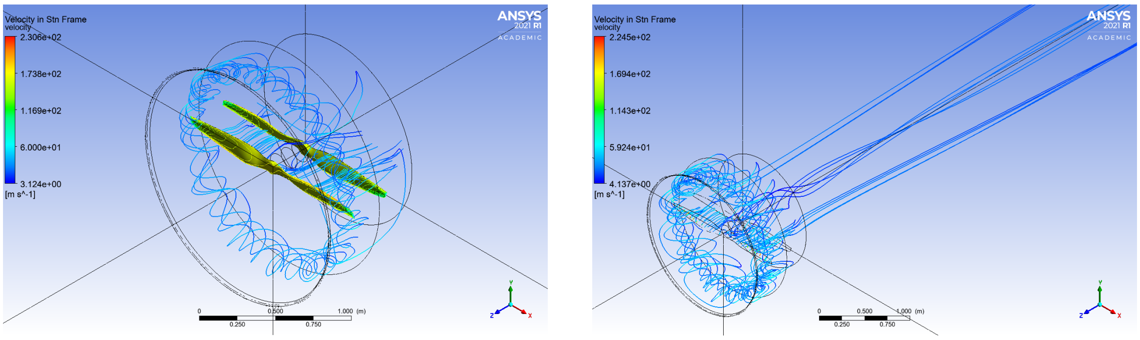

(a) Shrouded propellers, velocity streamlines from front propeller

(b) Shrouded propellers, velocity streamlines through duct

Figure 4.27: Shrouded propeller velocity streamline plot

The simulations for shrouded propellers may not be completely valid, due to the lack of tip refinement. Much of the airflow detail occurs near the tips, and this may not be adequately captured with the current meshing and simulation parameters extended from the non-shrouded cases. A transient simulation may also be useful in capturing flow properties more accurately, if there is a lot of dynamic interaction with shroud walls.

Now that it has has been established that the unshrouded coaxial propellers can produce the required thrust to lift a third of the maximum take-off weight, the question of efficiency comes in. Since the range of the ambulance would be critical to ensure that the patient would get to a location where aid can be administered, how efficiently the UAM vehicle's propulsion system uses power needs to be investigated.

4.4 Propulsion Efficiency

The Figure of Merit, as defined in the theory section (2.14), helps evaluate the propulsive efficiency using equation 2.14b, which relies on the power input required. The simulation results for both single propeller and coaxial configurations can be seen in figure 4.28.

Aside from the anomalous value in the single propeller plot (likely due to the use of the adjustment factor), the larger Mejzlik propeller generally has a higher figure of merit than the T-motor model. This is in line with the general trend that larger propellers are more efficient, as their larger diameter allows them to act on more air at once per rotation from the larger swept area. It can also be seen that coaxial propeller propulsion is more efficient than the single propeller system, and this is more evident for the Mejzlik propeller than the T-motor one.

There is a peak efficiency that can be observed in the curves for the Mejzlik propeller, it is uncertain whether the T-motor propeller has reached this efficiency peak, as there is insufficient data. Since the manufacturer states that the maximum thrust can be up to 11 kg, more simulations can be conducted to determine at what thrust level the actual peak efficiency occurs.

Comparisons to manufacturer data reveal that the manufacturers' data predicts a

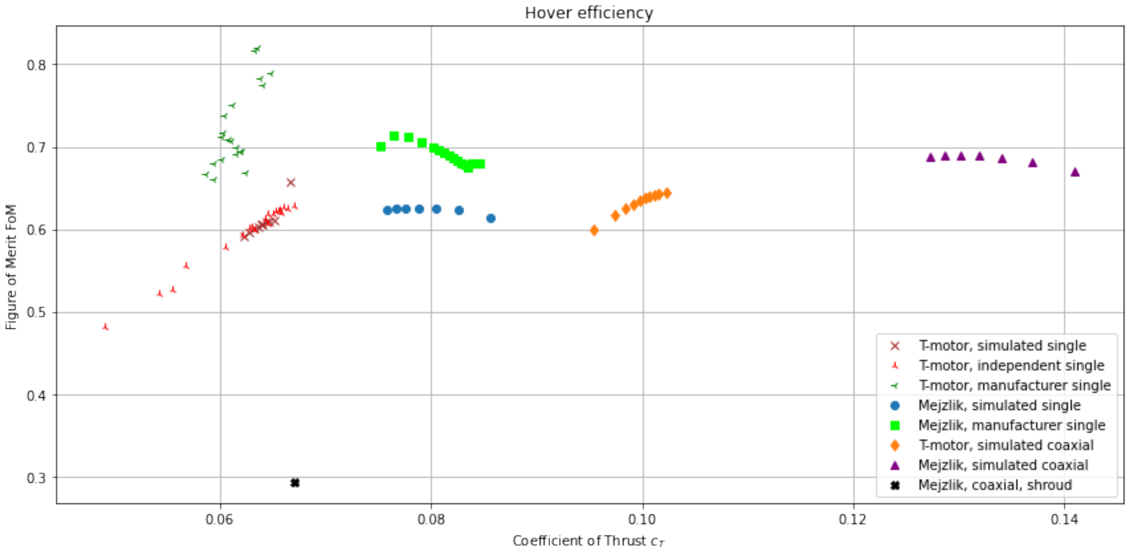

Figure 4.28: Hover efficiency

higher efficiency than simulations. However, the independent testing data for the T-Motor propeller shows that the simulation data is more accurate than manufacturer data-based predictions. This cannot also be said for the Mejzlik propeller, since the data is not available, but it is likely to be true, given the relative accuracy of the simulations for the T-Motor propeller to experimental data.

The single data point does not bode well for the ducted propellers, as it shows abysmal efficiency in hover compared to all other cases investigated.

In terms of optimising propeller efficiency, there will have to be a trade-off between weight and torque requirements when it comes to propeller selection. More blades will result in lower propeller efficiency from blade interference, but produce greater thrust, and a larger propeller, though more efficient, requires more power due to increased torque requirements. Another factor that needs to be considered is that the tip speed increases with larger diameters, and past Mach 0.8, transonic compressibility losses from wave drag become a major factor [31]. Wave drag was not investigated in the simulations, so it is unknown whether the present simulation setup will demonstrate these losses effectively, but they will need to be kept in mind when selecting larger propellers.

4.5 Tip Speed

A plot of tip Mach numbers can give one a sense of the risk of incurring transonic losses. This can be found in figure 4.29 for both propellers investigated.

The Mejzlik propeller is very close to the region where wave drag becomes a major source of loss, and to produce the required thrust for hover at this point means setting the 60% load at a point where increased thrust to increase altitude greatly decrease efficiency and decrease vehicle range. This could be mitigated by increasing propeller diameter or number of blades, and an optimisation analysis would have to be conducted to determine which trade-off is more acceptable.

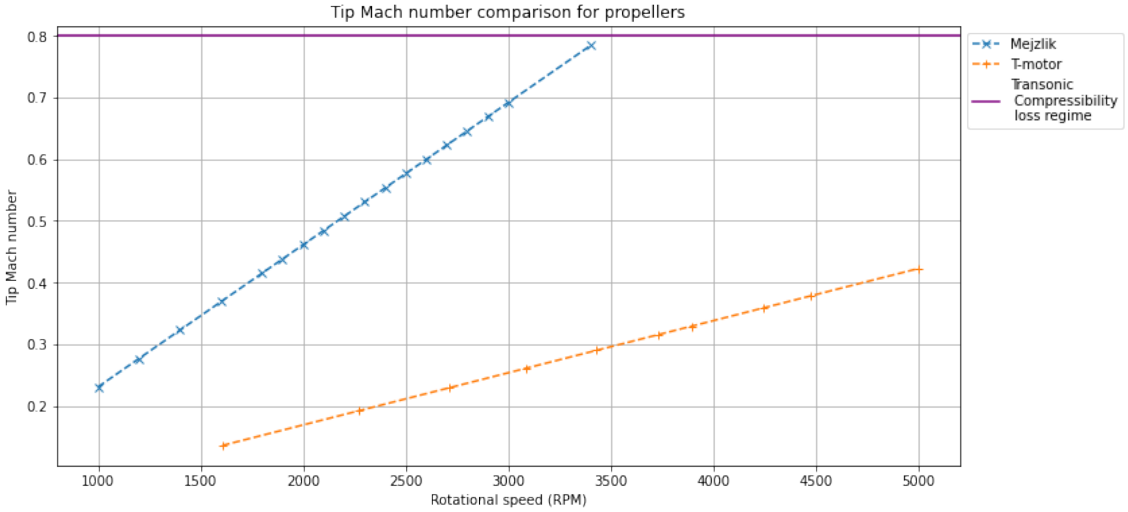

Figure 4.29: Tip speed

The T-motor propeller, on the other hand, is not close to the wave drag loss region and can be spun much faster (approximately 9500 RPM) before it approaches Mach 0.8 at the tips and starts to suffer significant wave drag losses. This means the largest limiting factor in producing more thrust is the motor used to drive the propellers, as observed from the model used during experiments, both from overheating, and power supply limits placed by the motor on itself to prevent damage. A motor that can provide the required torque to spin the propeller for hover performance at 60% propulsion load could be selected and the current propeller would be able to fulfil its role in the small-scale demonstrator.

While the ducted propeller only has one data point, it shows very underwhelming performance. This cannot be reflective of ducts over propellers as a whole, because a similar principle is used on many aircraft propulsion systems such as high bypass turbofan engines to great effect, and must lie in the design of the duct, as seen in the results presented. An investigation of a proper shroud design must be conducted to conclusively decide if the inclusion of a duct is worth the effort, but that would take much time, and hence was not the scope of this investigation despite the title of the report.

4.6 Suggestions for further investigation

While this report has been able to make a conclusion for the question that drove the investigation on whether the numerical investigations could predict the performance of the prop, there is more information that could be gained that can be used to drive propeller selection and improve the investigation methodology. Some of these suggestions include:

- Simulate up to manufacturer recommended RPM limit for T-motor propeller
- Complete a full shroud design cycle and test, as originally intended for this investigation
- Obtain another 3D model of the T-motor propeller using another scanning

method for comparison
- Use improved meshes and rotational symmetry to reduce computation resources
- Simulate transient flow for coaxial propellers to determine if there are differences
- Test using a smaller or higher pitch rear propeller to improve system efficiency

5

Conclusion

From the data obtained over the course of the investigations, there are improvements to be made to the investigation methodology, but a conclusion of whether the investigated propellers can work for their intended purpose can be made.
The investigation shows that while the propellers tested can produce the required thrust levels in the test conditions for the two different vehicle prototypes. However, for the large scale prototype, the rotational speed at which the propeller produces the requisite thrust is close to the boundary for transonic wave drag penalties, and additional speed will significantly decrease efficiency of the propulsive system, decreasing range and maneuverability to the point of ineffectuality of the air ambulance. An alternate propeller that can produce this thrust at lower Mach numbers is required, so that there is spare power envelope for additional operations other than hovering. Simulations reveal that comprehensive duct design and testing is required so that a shroud does not decrease the performance of propellers, as observed from the data in this report.
The small scale systems prototype has potential to fulfil its purpose for the required operating conditions, with the use of an appropriate power delivery system and motor. More data would be useful, but not necessary to solidify the conclusions from numerical analysis of the propeller.

Bibliography

[1] Elizabeth Ciobanu. *Average Weights of Common Types of Drones - Droneblog.* [Online; accessed 27. Jun. 2024]. June 2021. URL: `https://www.droneblog.com/average-weights-of-common-types-of-drones`.

[2] Klas Sjöberg. *Svensk Luftambulans.* [Online; accessed 26. Jun. 2024]. Aug. 2022. URL: `https://svenskluftambulans.se/app/uploads/2023/03/Helikopter-Lycksele-220316-Foto-Klas-Sjoberg_webb-1.jpg`.

[3] Boeing. *H-47 Chinook.* [Online; accessed 27. Jun. 2024]. June 2024. URL: `https://www.boeing.com/defense/ch-47-chinook#overview`.

[4] T-DRONES. *MX860 Multirotor Industrial Drone Products - T-DRONES.* [Online; accessed 17. Jun. 2024]. June 2024. URL: `https://www.t-drones.com/product/MX860.html`.

[5] Andrey Mossejev. *Tupolev Tu-95 - Wikipedia.* [Online; accessed 26. Jun. 2024]. Aug. 2007. URL: `https://en.wikipedia.org/w/index.php?title=Tupolev_Tu-95&oldid=1226985599`.

[6] Vlsergey. *Kamov Ka-52 - Wikipedia.* [Online; accessed 26. Jun. 2024]. Aug. 2009. URL: `https://en.wikipedia.org/w/index.php?title=Kamov_Ka-50&oldid=1228053609`.

[7] Alexandre Capitao Patrao. "On the Aerodynamic Design of the Boxprop". PhD thesis. Sweden: Chalmers University of Technology, 2018. ISBN: 978-91-7597-795-9. eprint: `505742`. URL: `https://research.chalmers.se/en/publication/505742`.

[8] Mateusz Stajuda et al. "Development of a CFD model for propeller simulation." In: *Mechanics & Mechanical Engineering* 20.4 (2016).

[9] Eric Vargas Loureiro et al. "Evaluation of low fidelity and CFD methods for the aerodynamic performance of a small propeller". In: *Aerospace Science and Technology* 108 (2021), p. 106402. ISSN: 1270-9638. DOI: `https://doi.org/10.1016/j.ast.2020.106402`. URL: `https://www.sciencedirect.com/science/article/pii/S1270963820310841`.

[10] Hairuniza Ahmed Kutty and Parvathy Rajendran. "3D CFD simulation and experimental validation of small APC slow flyer propeller blade". In: *Aerospace* 4.1 (2017), p. 10.

[11] Balram Panjwani et al. "Virtual Modelling and Testing of the Single and Contra-Rotating Co-Axial Propeller". In: *Drones* 4.3 (2020). ISSN: 2504-446X. DOI: `10.3390/drones4030042`. URL: `https://www.mdpi.com/2504-446X/4/3/42`.

[12] Clovis R. Maliska. *Fundamentals of Computational Fluid Dynamics.* Cham, Switzerland: Springer International Publishing, 2023. ISBN: 978-3-031-18235-

8. URL: `https://link.springer.com/book/10.1007/978-3-031-18235-8#back-to-top`.

[13] Woods Hole Oceanographic Institution. *Rotating Coordinate Systems and the Equations of Motion.* [Online; accessed 5. Jul. 2024]. July 2007. URL: `https://www.whoi.edu/cms/files/12.800_Chapter_4_%2706_25333.pdf`.

[14] J. D. Denton and U. K. Singh. *Time marching methods for turbomachinery flow calculation.* In Von Karman Inst. for Fluid Dyn. Appl. of Numerical Methods to Flow Calculations in Turbomachines 47 p (SEE N80-12365 03-34). Jan. 1979.

[15] F. R. Menter. “Two-equation eddy-viscosity turbulence models for engineering applications”. In: *AIAA Journal* 32.8 (1994), pp. 1598–1605. DOI: `10.2514/3.12149`. eprint: `https://doi.org/10.2514/3.12149`. URL: `https://doi.org/10.2514/3.12149`.

[16] Sal Rodriguez. *Applied Computational Fluid Dynamics and Turbulence Modeling.* Cham, Switzerland: Springer International Publishing, 2019. ISBN: 978-3-030-28691-0. URL: `https://link.springer.com/book/10.1007/978-3-030-28691-0`.

[17] Z. S. Spakovszky. *11.7 Performance of Propellers.* [Online; accessed 17. Jul. 2024]. Sept. 2008. URL: `https://web.mit.edu/16.unified/www/FALL/thermodynamics/notes/node86.html`.

[18] Tin-Chee Wong. “The Impact of Advanced Airfoils on Rotor Hover Performance”. In: *26th AIAA Applied Aerodynamics Conference.* 2008, p. 7342.

[19] Colin P. Coleman. *A Survey of Theoretical and Experimental Coaxial Rotor Aerodynamic Research.* [Online; accessed 18. Jul. 2024]. Jan. 1997. URL: `https://ntrs.nasa.gov/citations/19970015550`.

[20] Gordon J Leishman. *Principles of helicopter aerodynamics with CD extra.* Cambridge university press, 2006.

[21] J Gordon Leishman and Monica Syal. “Figure of merit definition for coaxial rotors”. In: *Journal of the American Helicopter Society* 53.3 (2008), pp. 290–300.

[22] *NS22x6.6 Prop - T-MOTOR Store.* [Online; accessed 18. Jul. 2024]. July 2024. URL: `https://store.tmotor.com/product/ns22x6_6-prop-uav-carbon-fiber.html`.

[23] Mejzlik Propellers. *Propeller 60x21 CCW 2B MC - Mejzlik Propellers.* [Online; accessed 18. Jul. 2024]. July 2024. URL: `https://shop.mejzlik.eu/propeller-60x21-ccw-2b-mc`.

[24] Rick. *T-Motor MN501S-240 with T-Motor NS22x66 test data.* [Online; accessed 18. Jul. 2024]. Aug. 2021. URL: `https://database.tytorobotics.com/tests/gyyq/t-motor-mn501s-240-with-t-motor-ns22x66`.

[25] John F Groeneweg and Lawrence J Bober. *NASA advanced propeller research.* Tech. rep. NASA, 1988.

[26] Intertechnology Inc. [Online; accessed 31. Jul. 2024]. Nov. 2016. URL: `https://www.vishay-loadcells-intertechnology.com/pdf/tedea/single-point/1042.pdf`.

[27] GW Instek. *GDM-8342 & GDM-8341 Dual Measurement Multimeter*. [Online; accessed 23. Aug. 2024]. 2021. URL: `https://www.gwinstek.com/en-global/products/detail/GDM-8342_GDM-8341`.

[28] Rigol Technologies Inc. *DHO800 Compact Size, Various Interfaces | RIGOL*. [Online; accessed 23. Aug. 2024]. 2024. URL: `https://www.rigolna.com/products/rigol-digital-oscilloscopes/dho800`.

[29] NASA. *Propeller Thrust | Glenn Research Center | NASA*. [Online; accessed 22. Aug. 2024]. July 2024. URL: `https://www1.grc.nasa.gov/beginners-guide-to-aeronautics/propeller-thrust`.

[30] T-MOTOR. *NS22x6.6 - NSUltra Light - T-MOTOR The Safer Propulsion System — uav-en.tmotor.com*. `https://uav-en.tmotor.com/2020/NS_0117/321.html`. [Accessed 06-08-2024]. 2018.

[31] SKYbrary Aviation Safety. *Propeller | SKYbrary Aviation Safety — skybrary.aero*. `https://skybrary.aero/articles/propeller`. [Accessed 06-08-2024].

A

Appendix 1 - T-Motor NS 22x6.6 Performance Data

The data here is the raw propeller performance data compiled from various sources, and from which all other data is derived for the T-Motor NS 22x6.6 Propeller.

A.1 Manufacturer Performance Data

The data contained here is obtained from T-motor's own performance metrics, found at `https://store.tmotor.com/product/mn505-s-kv320-motor-navigator-type.html`.

Table A.1: Manufacturer performance data for T-motor propeller

Type	Propeller	Throttle	Voltage (V)	Thrust (g)	Torque (N*m)	Current (A)	RPM
MN505S KV320	T-MOTOR P22*6.6	40%	24.01	1424	0.27	5.5	2573
		42%	24.02	1525	0.29	6.1	2668
		44%	24.01	1657	0.33	6.7	2770
		46%	24.01	1788	0.36	7.5	2873
		48%	24.01	1959	0.39	8.3	2990
		50%	24.00	2090	0.43	9.2	3197
		52%	24.00	2267	0.46	10.3	3312
		54%	24.00	2413	0.51	11.4	3439
		56%	24.00	2586	0.55	12.6	3565
		58%	23.99	2799	0.60	14.0	3689
		60%	23.99	2968	0.64	15.2	3790
		62%	23.99	3149	0.69	16.6	3888
		64%	23.98	3298	0.73	17.9	3980
		66%	23.97	3477	0.77	19.3	4071
		68%	23.97	3665	0.81	20.9	4182
		70%	23.96	3843	0.85	22.2	4375
		75%	23.95	4349	0.96	26.7	4623
		80%	23.94	4828	1.08	31.0	4936
		90%	23.90	5747	1.31	41.1	5346
		100%	23.87	6680	1.54	52.4	5625

Continued on next page

Table A.1: Manufacturer performance data for T-motor propeller

Power (W)	Efficiency (g/W)	Operating Temperature (°C)
132	10.83	88.5 (Ambient Temperature: 9.5)
145	10.49	
162	10.24	
180	9.95	
200	9.79	
221	9.46	
246	9.20	
272	8.86	
301	8.59	
335	8.36	
364	8.15	
398	7.90	
429	7.69	
464	7.50	
500	7.33	
533	7.21	
640	6.80	
743	6.50	
983	5.85	
1249	5.35	

A.2 Independent Test Data

The data contained here is obtained from independent testing, found at Tyto Robotics' motor and propeller database (`https://database.tytorobotics.com/tests/gyyq/t-motor-mn501s-240-with-t-motor-ns22x66`).

Table A.2: Independent test data for T-motor propeller

Time (s)	Throttle (µs)	Rotation speed (rpm)	Thrust (kgf)	Torque (N·m)	Voltage (V)	Current (A)	Electrical power (W)
1.24	1000	0.0	-0.00	0.00	25.04	-0.03	0.72
18.77	1991	4471.0	4.53	1.15	23.61	29.68	700.84
23.74	1943	4354.0	4.26	1.08	23.65	27.03	639.18
28.72	1896	4241.0	4.02	1.02	23.70	24.68	585.00
33.69	1849	4078.0	3.70	0.94	23.78	22.09	525.27
38.69	1802	3893.0	3.36	0.85	23.91	18.68	446.60
43.67	1754	3727.0	3.08	0.78	24.01	16.22	389.48
48.64	1707	3596.0	2.85	0.72	24.09	14.39	346.69
53.62	1660	3429.0	2.60	0.66	24.18	12.45	301.11
58.60	1612	3267.0	2.33	0.59	24.27	10.51	254.98
63.62	1565	3084.0	2.07	0.53	24.35	8.83	215.11
68.61	1518	2871.0	1.80	0.46	24.43	7.19	175.59
73.60	1471	2714.0	1.56	0.40	24.49	5.93	145.28
78.63	1423	2491.0	1.33	0.34	24.56	4.66	114.42
83.77	1376	2273.0	1.10	0.28	24.62	3.55	87.40
88.87	1329	2065.0	0.90	0.23	24.66	2.69	66.46
93.87	1281	1838.0	0.69	0.18	24.71	1.91	47.31
98.92	1234	1606.0	0.48	0.13	24.75	1.29	32.05

Continued on following page

Continued on next page

Table A.2: Independent test data for T-motor propeller

Time (s)	Throttle (µs)	Rotation speed (rpm)	Thrust (kgf)	Torque (N·m)	Voltage (V)	Current (A)	Electrical power (W)
104.01	1187	1370.0	0.36	0.10	24.77	0.84	20.83
109.03	1140	1119.0	0.23	0.06	24.80	0.52	12.93
114.15	1092	836.0	0.12	0.03	24.81	0.28	6.87

Table A.2: Independent test data for T-motor propeller

Mechanical power (W)	Motor & ESC efficiency (%)	Propeller efficiency (gf/W)	Propulsion system efficiency (gf/W)
0.00	0.00	NaN	NaN
538.52	76.84	8.41	6.47
493.64	77.23	8.63	6.66
451.74	77.22	8.90	6.87
403.26	76.77	9.18	7.05
348.24	77.98	9.65	7.52
305.22	78.37	10.11	7.92
272.40	78.57	10.45	8.21
236.49	78.54	10.99	8.63
202.00	79.22	11.53	9.13
170.50	79.26	12.13	9.61
139.36	79.37	12.90	10.24
114.35	78.71	13.68	10.77
89.90	78.57	14.79	11.62
67.31	77.01	16.36	12.60
50.24	75.59	17.84	13.49
34.87	73.71	19.82	14.61
22.46	70.07	21.58	15.12
13.68	65.70	26.33	17.30
7.40	57.21	31.05	17.76
2.88	41.89	40.31	16.89

A.3 Coaxial Experimental Data

The data contained here is obtained from from in-house testing of the propeller, using the setup described in section 3.2.

Table A.3: Coaxial experimental data for T-Motor propeller

Thrust (N)	RPM Upper	RPM Lower
1.64	654.50	661.55
16.04	2234.92	2324.32
43.94	3818.83	3619.52
76.79	4633.68	4988.43
91.04	5402.09	5388.33

A.4 Simulation Data

The data contained here is from simulations conducted using a scanned model of the propeller, and analysed using ANSYS CFX, from which all other data was derived, in conjunction with the other data tables contained here.

Table A.4: Simulation data for T-Motor propeller

RPM	Single Propeller		Coaxial			
	Thrust (N)	Torque (Nm)	Front thrust (N)	Rear thrust (N)	Front torque (Nm)	Rear torque (Nm)
1606.00	4.88	0.12	4.54	2.45	0.13	0.11
2273.00	9.14	0.25	9.25	5.03	0.25	0.22
2714.00	13.14	0.36	13.29	7.28	0.36	0.31
3084.00	17.07	0.47	17.28	9.49	0.47	0.40
3429.00	21.22	0.58	21.48	11.83	0.58	0.50
3727.00	25.19	0.68	25.49	14.06	0.69	0.59
3893.00	27.56	0.75	27.89	15.40	0.75	0.65
4241.00	32.87	0.89	33.27	18.39	0.89	0.77
4471.00	36.66	1.00	37.10	20.51	1.00	0.86
5000.00	46.19	1.26	46.74	25.87	1.26	1.09

B

Appendix 2 - Mejzlik Propellers 60x21 Performance Data

The data here is the raw propeller performance data compiled from various sources, and from which all other data is derived for the Mejzlik Propellers Propeller 60x21 2B MC.

B.1 Manufacturer Performance Data

The data contained here is obtained from Mejzlik's own performance metrics, provided by them along with the CAD model.

Table B.1: Manufacturer performance data for Mejzlik propeller

RPM	Thrust (N)	Thrsut (kg)	Torque (Nm)	Mech. Power (W)	Tip speed (m/s)	Mach
1000	138.015176	14.073631	9.253497	969.023923	79.796453	0.234695
1200	202.209748	20.619656	13.451469	1690.361502	95.755744	0.281635
1400	280.150062	28.567356	18.835550	2761.435919	111.715035	0.328574
1600	371.836118	37.916732	25.405740	4256.772564	127.674325	0.375513
1800	477.267916	48.667783	33.162038	6250.896824	143.633616	0.422452
1900	535.138469	54.568937	37.484977	7458.293494	151.613261	0.445921
2000	596.445457	60.820510	42.104444	8818.334088	159.592907	0.469391
2100	661.188880	67.422502	47.020438	10340.334280	167.572552	0.492860
2200	729.368739	74.374913	52.232958	12033.609745	175.552197	0.516330
2300	800.985034	81.677743	57.742006	13907.476154	183.531843	0.539800
2400	876.037764	89.330991	63.547581	15971.249183	191.511488	0.563269
2500	954.526930	97.334659	69.649684	18234.244504	199.491134	0.586739
2600	1036.452531	105.688745	76.048313	20705.777791	207.470779	0.610208
2700	1121.814213	114.393214	81.922373	23163.005140	215.450424	0.633678
2800	1210.612658	123.448136	88.597250	25978.070546	223.430070	0.657147
2900	1302.847538	132.853476	95.532179	29011.908481	231.409715	0.680617
3000	1398.518853	142.609235	102.727159	32272.688690	239.389360	0.704086

B.2 Simulation Data

The data contained here is from simulations conducted using a CAD model of the propeller provided by Mejzlik, and analysed using ANSYS CFX.

Table B.2: Simulation data for Mejzlik propeller

RPM	Single Propeller		Coaxial			
	Thrust (N)	Torque (Nm)	Front thrust (N)	Rear thrust (N)	Front torque (Nm)	Rear torque (Nm)
1000.00	140.81	10.56	141.06	92.51	10.63	10.13
1400.00	279.02	20.99	279.51	183.49	21.14	20.14
1800.00	467.00	35.30	467.50	306.54	35.54	33.83
2200.00	708.55	53.93	709.26	462.67	54.29	51.59
2600.00	1009.33	77.63	1009.78	654.05	78.11	74.04
3000.00	1380.84	107.87	1379.52	883.39	108.35	102.24
3400.00	1838.58	148.69	1834.24	1156.96	148.51	138.80

Table B.3: Shrouded simulation data for Mejzlik propeller

RPM	Front thrust (N)	Rear thrust (N)	Front torque (Nm)	Rear torque (Nm)
3000.0	385.472	721.768	57.4372	109.882

DEPARTMENT OF SOME SUBJECT OR TECHNOLOGY
CHALMERS UNIVERSITY OF TECHNOLOGY
Gothenburg, Sweden
www.chalmers.se

CHALMERS
UNIVERSITY OF TECHNOLOGY